ADVANCED ENERGY MATERIALS
www.advenergymat.de

Insights into the Jahn-Teller Effect in Layered Oxide Cathode Materials for Potassium-Ion Batteries

Yunshan Zheng, Huixian Xie, Junfeng Li, Kwan San Hui, Zhenjiang Yu, Huifang Xu, Duc Anh Dinh, Zhengqing Ye, Chenyang Zha, and Kwun Nam Hui**

Potassium-ion batteries (PIBs) have attracted increasing interest as promising alternatives to lithium-ion batteries (LIBs) in large-scale electrical energy storage systems due to the potential price advantages, abundant availability of potassium resources, and low standard redox potential of potassium. However, the pursuit of suitable cathode materials that exhibit desirable characteristics such as voltage platforms, high capacity, and long cycling stability is of utmost importance. Recently, layered transition-metal oxides for PIBs offer great potential due to their high theoretical capacity, suitable voltage range, and eco-friendliness. Nevertheless, the progress of K_xMO_2 cathodes in PIBs faces obstacles due to the detrimental effects of structural disorder and irreversible phase transitions caused by the Jahn-Teller effect. This review provides a brief description of the origin and mechanism of the Jahn-Teller effect, accompanied by the proposed principles to mitigate this phenomenon. In particular, the current status of K_xMO_2 cathodes for PIBs, is summarized highlighting the challenges posed by the Jahn-Teller effect. Furthermore, promising strategies, such as composition modulation, synthesis approaches, and surface modification, are proposed to alleviate and suppress the Jahn-Teller effect. These strategies offer valuable insights into the prospects of innovative cathode materials and provide a foundation for future research in the field of PIBs.

1. Introduction

Over the past few decades, significant advancements in lithium-ion batteries (LIBs) have been witnessed by the research community, primarily attributed to their extensive driving range. However, the expanding applications of energy storage face challenges due to the limited and uneven distribution of lithium resources in the Earth's crust, resulting in increased manufacturing costs for LIBs. To address this issue, sodium-ion batteries (SIBs) and potassium-ion batteries (PIBs) have emerged as two promising alternatives. These alternatives utilize more abundant resources and share intercalation chemistry with LIBs. Notably, PIBs are considered superior to LIBs due to their abundant and low-cost resources, along with a comparable standard redox potential of K/K^+ (−2.936 V vs SHE), enabling high operating voltage and energy density.[1–3] In addition to high voltage operation, fast K^+ ion diffusion in PIBs also contributes to higher power capability.[4] By comparing the ionic and Stokes radius of Li^+, Na^+, and K^+ ions in PC (propylene carbonate), the K^+ ions exhibit the smallest Stokes radius among the studied ions in PC solutions, despite the fact that the K^+ ion has the largest ionic radius. To date, numerous research efforts have been undertaken to develop safe PIBs. Extensive research has focused on cathodes as a crucial component of PIBs. The positive electrode materials that have been documented can be classified into various material categories, including transition metal layered oxides,[4–10] prussian blue analogs (PBAs),[11] polyanionic

Y. Zheng, H. Xie, J. Li, Z. Yu, H. Xu, C. Zha, K. N. Hui
Joint Key Laboratory of the Ministry of Education
Institute of Applied Physics and Materials Engineering
University of Macau
Avenida da Universidade, Taipa, Macau SAR 519000, P. R. China
E-mail: bizhui@um.edu.mo

The ORCID identification number(s) for the author(s) of this article can be found under https://doi.org/10.1002/aenm.202400461

DOI: 10.1002/aenm.202400461

K. S. Hui
School of Engineering
Faculty of Science
University of East Anglia
Norwich NR4 7TJ, UK
E-mail: k.hui@uea.ac.uk

D. A. Dinh
VKTech Research Center
NTT Hi-Tech Institute
Nguyen Tat Thanh University
Ho Chi Minh City 700000, Vietnam

Z. Ye
Tianjin Key Laboratory of Materials Laminating Fabrication and Interface Control Technology
School of Material Science and Engineering
Hebei University of Technology
Tianjin 300401, P. R. China

compounds,[12] and organic materials.[13] **Figure 1a** illustrates the specific capacity versus redox voltage data for various PIB cathode materials. Despite polyanionic compounds exhibiting lower specific capacities, their average discharge redox voltages consistently surpass those of other cathode material categories.

Among various options, transition metal layered oxides K_xMO_2 (M = Mn, Cr, Fe) are regarded as the most promising cathode materials due to their high theoretical capacity, suitable working voltage, exceptional rate performance, high tap density, straightforward preparation method, low-cost, and environmental friendliness (Figure 1b–e).[4–10,14] Regrettably, the initial stage of K_xMO_2 development failed to adequately address several limitations, including inferior cyclic stability, voltage decay, and structural degradation. These challenges have significantly impeded the practical implementation of K_xMO_2. Of particular concern is the adverse impact of the Jahn-Teller effect on K_xMO_2, leading to structural deterioration during electrochemical processes.[9,15–21]

The presence of high-spin Mn^{3+}/ high-spin Fe^{4+}/Cr^{2+} in the octahedral MO_6 units of K_xMO_2 leads to a severe Jahn-Teller effect, which negatively impacts the structural stability and electrochemical properties of the material.[4,22] To address this issue, several effective strategies have been proposed to alleviate the Jahn-Teller effect and enhance the electrochemical performance of K_xMO_2. These include TM element substitution/doping and structural design. Lei et al.[23] demonstrated the in situ formation of a dual interface on the P2-$K_{0.67}MnO_2$ cathode, which consists of a solid-electrolyte interphase (SEI) formed on the P2-KMO and a K-poor spinel interlayer. This approach effectively mitigates the Jahn-Teller distortion, mitigating Mn^{2+} dissolution, and improving K^+ diffusion kinetics. Zhao et al.[3] employed a surface coating of AlF_3 on $K_{1.39}Mn_3O_6$ microspheres to improve their electrochemical performance. Once the detrimental effects stemming from the Jahn-Teller effect are successfully mitigated, a significant improvement in the overall performance of K_xMO_2 can be expected.[9,15,16]

In this review, we present a comprehensive overview of representative K_xMO_2 cathodes for PIBs. First, we present a concise explanation of the origin and mechanism of the Jahn-Teller effect, emphasizing its specific principles for mitigating this phenomenon. Subsequently, we delve into a detailed classification of K_xMO_2 cathodes and highlight the detrimental effects arising from the Jahn-Teller effect. Finally, we propose viable strategies, including composition modulation, structural design, synthesis strategies, and surface modification, aimed at alleviating the Jahn-Teller effect. These strategies offer valuable insights into the potential innovative cathode materials and future research in PIBs, ultimately facilitating their practical application in the large-scale energy storage (**Figure 2**).

2. Mechanisms and Challenges of Jahn-Teller Effect

The Jahn-Teller effect refers to a structural distortion in molecules or crystals that arises from the asymmetric distribution of electrons during the bonding process.[28] Essentially, the Jahn-Teller effect is a fundamental quantum mechanical phenomenon that is ubiquitous in molecules, ions, and solids.[29]

2.1. The Origin of Jahn-Teller

In 1937, Hermann Jahn and Edward Teller formulated a theorem stating that a non-linear molecular system in an electronic degenerate state will undergo distortion, which will remove the degeneracy, reduce the symmetry, and ultimately lower the total energy. This distortion results in the removal of degeneracy, a reduction in symmetry, and a subsequent decrease in the total energy of the system. Referred to as the Jahn-Teller distortion, this phenomenon gives rise to the broader concept known as the Jahn-Teller effect. The Jahn-Teller effect is responsible for reducing the symmetry of certain molecular geometries, leading to the stabilization of lower-energy states. This effect is particularly prominent in geometries such as tetrahedral and octahedral structures, and it specifically occurs in electronic configurations that include d-orbitals.[28,30–32] In the context of octahedral geometry, the Jahn-Teller effect induces a tetragonal elongation or compression, causing the displacement of ligands along the z-axis. This distortion preserves the inversion center while maintaining equidistant positioning of the two ligands along the z-axis from the center.[29,33,26d]

$$t_{2g}\ \text{orbitals} = d_{xy},\ d_{yz},\ d_{xz} \quad (1)$$

$$e_g\ \text{orbitals} = d_{x^2-y^2},\ d_{z^2} \quad (2)$$

In a non-linear molecular system experiencing electronic degeneracy, there is an uneven distribution of electrons within the d orbitals, specifically within the e_g set of orbitals ($d_{x^2-y^2}$ and d_{z^2}). This uneven distribution arises from the increased influence and repulsion exerted by ligands on the e_g orbitals in octahedral geometry. Unlike the t_{2g} set of orbitals, where ligands approach the central metal atom between the axes, in the e_g set, ligands approach the central metal atom along its axes. This distinction contributes to the asymmetry observed in the electronic distribution of the e_g set of orbitals.[29,34] The Jahn-Teller effect is prominently observed in metal ions coordinated in an octahedral fashion, particularly with electronic configurations of (high-spin) d^4, (low-spin) d^7, and d^9, where one of the e_g orbitals contains an unpaired electron. It is important to note that the Jahn-Teller theorem does not specify the direction of distortion (whether it will result in tetragonal compression or elongation). Instead, it predicts that distortion will inevitably take place in order to eliminate degeneracy and lower the overall energy of the system.[29,35] In octahedral geometry, when tetragonal compression or elongation occurs, it often leads to one of the orbitals in the e_g set ($d_{x^2-y^2}$ or d_{z^2}) becoming half-filled. Nonetheless, tetragonal elongation is the more common distortion observed in octahedral geometry.[36] The Jahn-Teller effect can also manifest in electrons in the t_{2g} set of orbitals (located in between the axes), which are positioned between the axes. However, due to the misalignment of these orbitals with the approaching ligands, the effect is generally less pronounced, leading to weaker Jahn-Teller distortions. Consequently, systems with electronic configurations such as d^1, d^2, low-spin d^4 and d^5, as well as, high-spin d^6 and d^7, electronic tend to exhibit weaker distortions in accordance with the Jahn-Teller effect.[34,37,38]

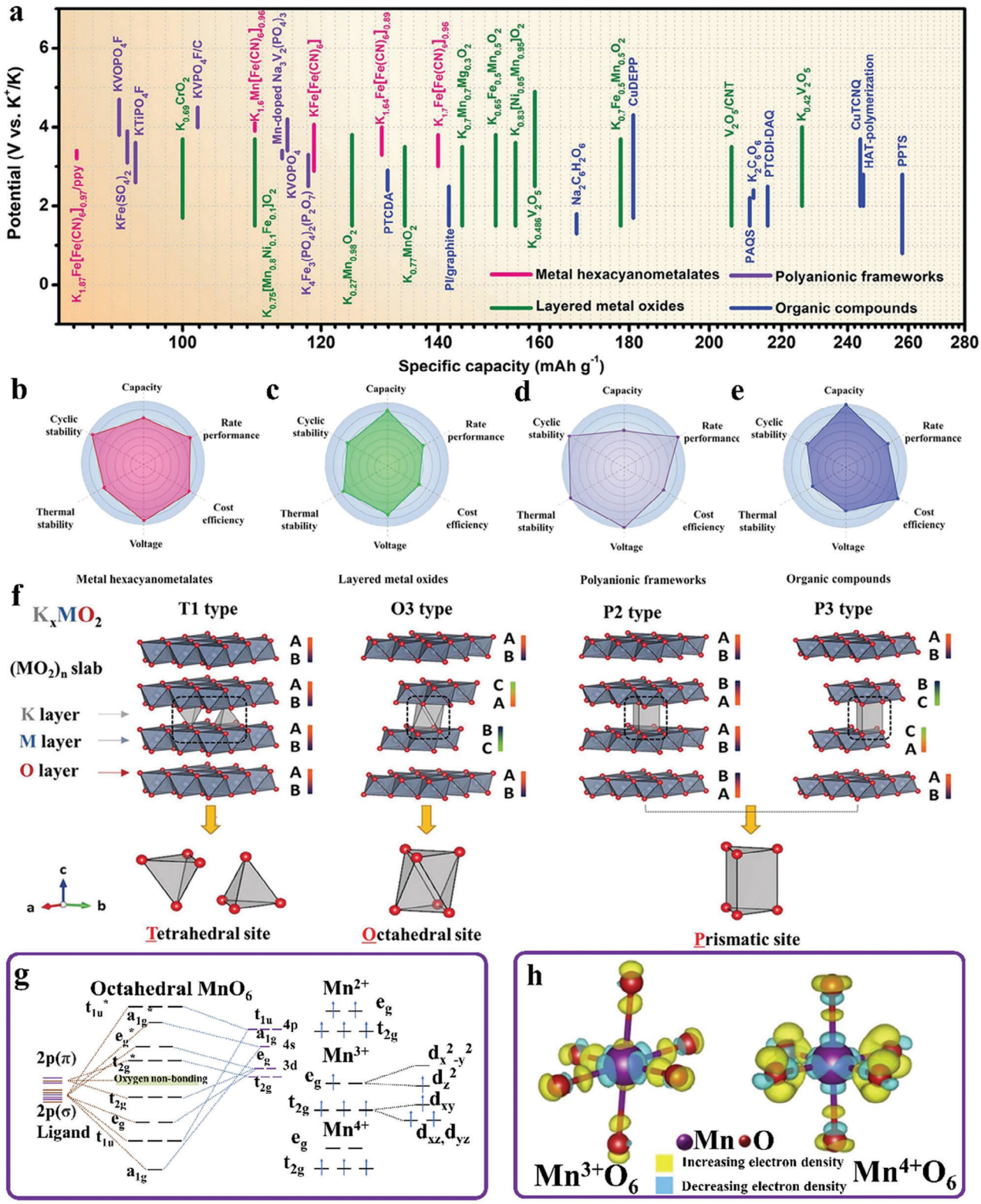

Figure 1. a) Comparison of specific capacities and average discharge redox voltages of various reported cathode materials. Radar plots charting useful metrics to assess. b) Metal hexacyanometalates. c) Layered metal oxides, d) Polyanionic frameworks, and e) Organic compounds. f) Crystal structures of T1, O3-, P3-, and P2-type layered metal oxides. a–f) Reproduced with permission.[24] Copyright 2021, Wiley-VCH. g) The molecular orbital energy diagram of the octahedral MnO_6 and the electronic orbitals of $Mn^{2+}/Mn^{3+}/Mn^{4+}$ ions. Reproduced with permission.[9] Copyright 2021, Elsevier. h) The calculated differential charge densities of the octahedral $Mn^{3+}O_6$ and $Mn^{4+}O_6$. Blue and yellow regions represent the decreasing and increasing electron density, respectively. The iso-surface of the charge density is set as 0.015 e $Bohr^{-1}$. Reproduced with permission.[25] Copyright 2020, Springer.

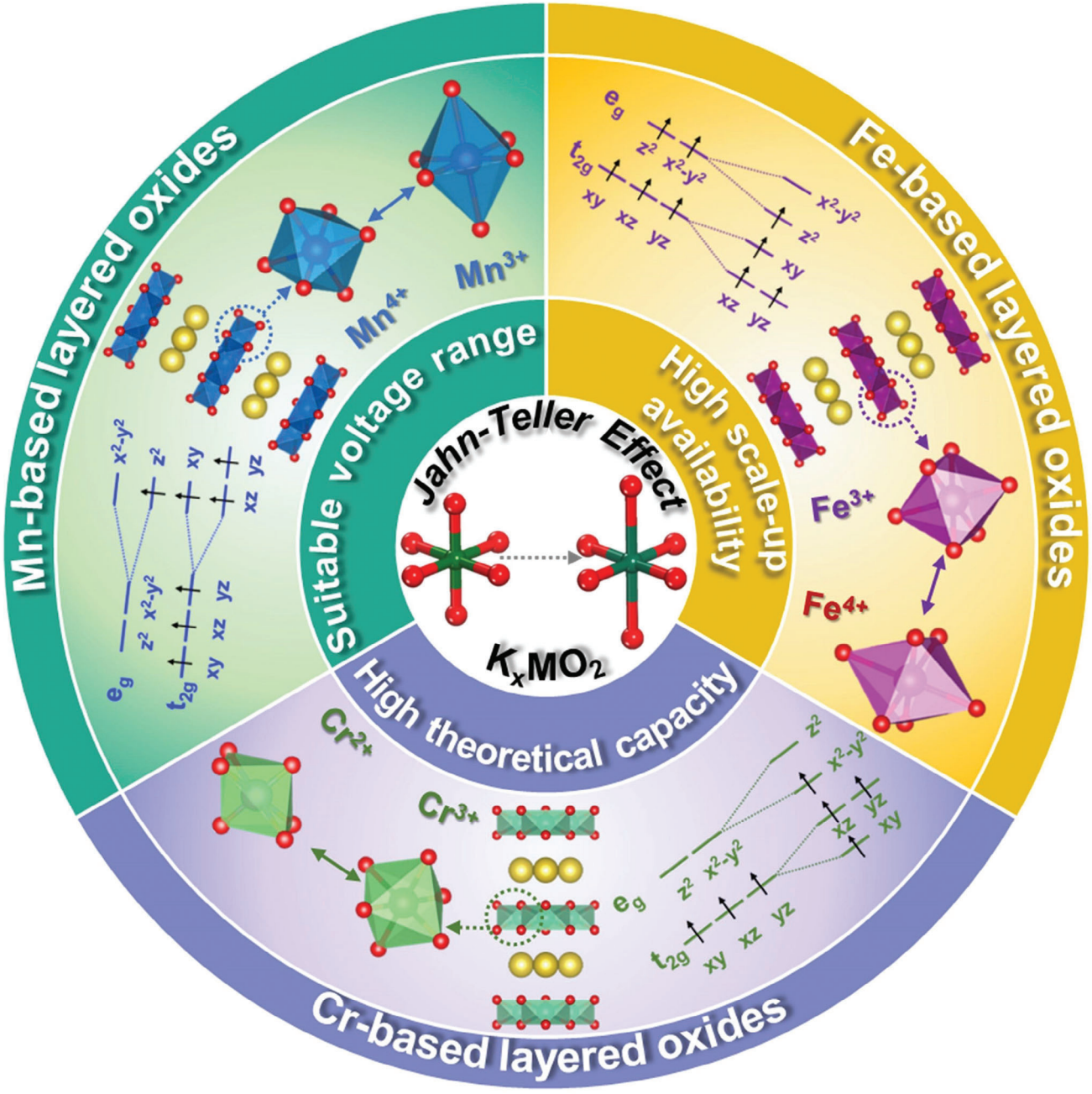

Figure 2. Schematic representation of layered metal oxide cathodes (including Mn/Cr/Fe layered metal oxides) that can be used in PIB systems, and the corresponding Jahn-Teller distortion summarized from the latest literature.[9,18,26,27]

2.2. Octahedral Complexes: Compression and Elongation Occur to Get Stability

Octahedral complexes undergo compression and elongation as a means to attain stability. During tetragonal compression, the energy of the $d_{x^2-y^2}$ orbital is lowered, while that of the d_{z^2} orbital is increased. When the ligands approach the central atom/ion along the z-axis, there is an increased repulsion between the electrons of the ligands and those in the d_{z^2} orbital. This causes the energy of the d_{z^2} orbital to increase and simultaneously decreases the energy of the $d_{x^2-y^2}$ orbital. However, the overall distortion leads to a stabilization effect, resulting in a reduction in the net energy of both orbitals.[33,38]

2.3. The Impact of Jahn-Teller Effect on Transition-Metal Compounds and Electrochemical Devices

It is worth highlighting that the Jahn-Teller effect arises from the fundamental a principles of quantum mechanics and is

observable in various chemical and physical systems. This effect is especially prominent in transition-metal (TM) compounds, where the presence of an odd number of electrons occupying the TM e_g orbital set (i.e., d_{z^2} and $d_{x^2-y^2}$) within an octahedral (O_h) ligand field often leads to a significant Jahn-Teller effect.[30,26d] In an idealized O_h ligand field, certain first-row TM ions exhibit a strong Jahn-Teller effect in the e_g band. Notable examples include Mn^{3+} (high spin, $t_{2g^3}e_{g^1}$), Fe^{4+} (high spin, $t_{2g^3}e_{g^1}$), and Cr^{2+}($t_{2g^3}e_{g^1}$).[30] The chemistry of these ions plays a critical role in various technological applications. For instance, the redox-active Mn^{3+}/Mn^{4+}, Fe^{3+}/Fe^{4+}, and Cr^{2+}/Cr^{3+} couples are widely employed in primary and secondary (rechargeable) batteries, which utilize both aqueous and non-aqueous electrolytes.[25,39] These advancements have ushered in a new era of high-performance energy storage and are paving the way for further developments in the field. However, it is important to address challenges associated with metal-ion dissolution and undesirable phase transformations, which are closely linked to Jahn-Teller (JT)-active transition metal oxides (TMOs) and have implications for the performance degradation of electrochemical devices. In the case of LIBs, for instance, the dissolution of transition metal ions and phase transformations occurring even at parts-per-million (ppm) levels of acidity in the electrolyte are recognized as the primary factors contributing to cell aging. Furthermore, the presence of JT-active Mn^{3+}/Ni^{3+}-containing oxides exacerbates the occurrence of phase transformations, leading to further degradation of performance.[30,26d]

3. The Jahn-Teller Effect in Layered Metal Oxides for PIBs

In the layered oxide structure, transition metal and alkali ions separate into alternating slabs that possess numerous 2D open frameworks, facilitating the migration of large K^+ ions.[9,19] Layered transition metal oxides are commonly represented using various symbols.[17,40] For instance, T, P, and O indicate the tetrahedral, prismatic or octahedral coordination environment of the K^+ ion, respectively. The number denotes the number of MO_2 slabs in the unit cell.[15,16] Figure 1f illustrates the schematic of the T1, O3, P3, and P2 crystal structures. Layered metal oxides of type T1 are not discussed in this review. In O3 crystals, all K^+ ions occupy octahedral sites, and the stacking of oxide layers follows the AB–CA–BC pattern.[4,41] At high K^+ concentrations, such as x = 1, the strong electrostatic K^+–K^+ repulsion destabilizes the K_xMO_2 layered compounds.[8,22] In P3 crystals, the oxide layer stacking follows the AB–BC–CA pattern, and K^+ ions occupy prismatic sites. P2 compounds result from AB–BA oxide layer stacking, and in P2 crystals, K^+ ions occupy distinct edge- or face-sharing prismatic sites. The prime symbol (') is utilized to indicate the in-plane distortion of hexagonal crystal lattices.[18,20] The P2-KMO_2 crystal structure refers a structure composed of prismatic K metal and MO_2 sheets. The following presented below represents the widely accepted reaction mechanism of layered transition metal oxides:[42]

$$KMO_2 \leftrightarrow K_{1-x}MO_2 + xK^+ + xe^- \quad (3)$$

During the charging and discharging process, the framework structure formed by MO_2 allows K^+ ions in both typical octahedral sites and prismatic sites, leading to a phase transformation.[43,44] The transformation from P3 to P2 phase occurs at high temperatures by breaking the M—O bonds. The electrochemical behaviors of layered compounds are influenced by the initial pristine compound's K^+-ion content and structural stability. In the extraction/insertion of K^+ ions, the O3 phase transitions to other phases as the MO_2 layer glides without breaking any M—O bonds. When a small amount of K^+ ions is extracted, the layer gliding causes a change in the oxide stacking pattern to the O3 to P3. This preference for prismatic sites over octahedral positions may be due to the larger K^+ ions and their energetically favorable occupancy. Neither O3 nor P3 materials can be electrochemically converted into P2 since the M—O bonds cannot be broken during charging and discharging. However, P2 materials can transform into O2 materials when the maximum K^+ ion concentration is extracted. Therefore, P compounds exhibit greater structural stability than O layered compounds due to fewer phase transitions.[24,43] Although these structures provide favorable pathways for ion migration, they are susceptible to the Jahn-Teller distortion, which can induce to lattice changes and compromise the stability of the crystal. Notably, the Jahn-Teller effect is observed in $Mn^{III}O_6$ octahedra (Mn^{3+}: $t_{2g^3}e_{g^1}$) upon deep discharge of K_xMnO_2.[45] The objective of this section is to investigate the influence of the Jahn-Teller distortion on layered metal oxides, with a particular focus on Mn/Fe/Cr-based layered oxides. By examining the specific manifestations and consequences of the Jahn-Teller effect in these layered structures, a comprehensive understanding of its impact on the electrochemical performance can be gained.

3.1. Mn-Based Layered Oxides

Manganese-based layered oxides have garnered considerable attention as promising cathode materials for PIBs due to their favorable properties. These include high theoretical capacity, the abundant of manganese, suitable voltage platform, excellent rate performance, high tap density, simple preparation method, and low cost.[7,46] However, the larger radius of K ions poses a significant challenge to the transport of K ions within K_xMnO_2 materials, resulting in a substantial decrease in power density. Additionally, the layered framework undergoes significant structural changes and distortions during K-ion de/intercalation. These factors, combined with the occurrence of severe side reactions with the electrolyte, further contribute to the decrease in capacity and cycling stability of the system.

In a groundbreaking study conducted by Vaalma et al.[47] non-aqueous PIBs utilizing layered $K_{0.3}MnO_2$ as the cathode material were successfully demonstrated. These PIBs exhibited an initial discharge capacity of 70 mAh g^{-1} and demonstrated reasonable capacity retention of 57% over 685 cycles at 27.9 mA g^{-1}, within the potential window of 1.5–3.5 V versus K/K^+. However, it is worth noting that the noticeable capacity fading was observed in $K_{0.3}MnO_2$ when operated under higher cutoff conditions (1.5–4.0 V). This fading could potentially be attributed to irreversible phase transitions occurring at elevated potentials. Since the pioneering work of Vaalma et al.[47] on the reversible storage of K-ions in $K_{0.3}MnO_2$, numerous studies have been conducted on similar compounds, such as $K_{0.5}MnO_2$, $K_{0.77}MnO_2{\cdot}0.23H_2O$.[6]

Manganese-based cathodes with P2/P3-type structures for K-ion batteries, specifically K_xMnO_2 (x = 0.3 and 0.45), were prepared using a simple co-precipitation method. Among these compounds, $K_{0.45}MnO_2$ demonstrates slightly superior performance compared to $K_{0.3}MnO_2$, with a reversible specific capacity of 128.6 mAh g^{-1} at 20 mA g^{-1}. Furthermore, $K_{0.45}MnO_2$ exhibits excellent rate performance, delivering a specific capacity of 51.2 mAh g^{-1} even at 200 mA g^{-1}.[48] In the study by Ceder et al., the P3-type $K_{0.5}MnO_2$ cathode material exhibited an initial discharge capacity of 140 mAh g^{-1} within the voltage range of 1.5–4.2 V at 5 mA g^{-1}. Furthermore, the capacity attenuation was only 30% after 20 cycles at 20 mA g^{-1}. However, the P3-$K_{0.5}MnO_2$ material exhibited poor rate capability, with a specific capacity of only 38 mAh g^{-1} at 300 mA g^{-1}.[8] The aforementioned issues primarily stem from the Jahn-Teller effect. The significant Jahn-Teller effect by MnO_6 octahedra, coupled with the large interslab distance in $KMnO_2$, makes the structure highly prone to collapse, especially when charged to high voltage ranges. This phenomenon leads to severe irreversibility and subsequent capacity loss.[49]

In octahedral MnO_6 fields, Mn^{3+} typically assumes a high-spin state with a large magnetic moment and exhibits collinear Jahn–Teller ordering of MnO_2 slabs along the elongated axes, resulting in a strong Jahn–Teller distortion. Regarding the electronic structures of 3d TMs, like Mn, the 3d orbitals are divided into doubly degenerate e_g orbitals (including $d_{x^2-y^2}$ and d_{z^2}) and triply degenerate t_{2g} orbitals (including d_{xy}, d_{xz}, and d_{yz}), as depicted in Figure 1g.[9] In an octahedral coordination, the high-spin Mn^{3+} cation ($t_{2g^3}e_{g^1}$) typically possesses a single electron occupying only one e_g orbital (e_{g^1}), leading to an asymmetric occupation state of the e_g orbitals. The distribution of electrons in the $d_{x^2-y^2}$ and d_{z^2} orbitals results in varying degrees of shielding effect on Mn nuclei in different directions. Consequently, the overall d orbitals no longer conform to the O_h symmetry of the octahedra, causing instability in the central Mn^{3+} cation. To stabilize the Mn^{3+} cation, the two longitudinal Mn—O bonds in the octahedral MnO_6 are elongated, while the other four horizontal Mn—O bonds are contracted. The Jahn-Teller effect induces a distortion in the MnO_6 octahedron, reducing its symmetry from O_h to D_{4h}. This distortion eliminates degenerate orbitals, lowers energy, and distorts the crystal structure. In particular, K_xMnO_2 systems containing high-spin Mn^{3+} ($t_{2g^3}e_{g^1}$) ions often exhibit poor electrochemical performance during cycling, which can be attributed to the Jahn-Teller effect. In contrast to Mn^{2+} and Mn^{4+}, the Jahn-Teller effect in Mn^{3+} is distinct due to its d electron configuration. Figure 1h illustrates the differential charge densities of the octahedral $Mn^{3+}O_6$ and $Mn^{4+}O_6$, as calculated using density functional theory (DFT). Unlike $Mn^{4+}O_6$, $Mn^{3+}O_6$ displays an occupied d_{z^2} orbital, indicated by the yellow regions adjacent to the central Mn^{3+} cation. This observation suggests that the Jahn-Teller distortion can be induced by high-spin Mn^{3+} but not by high-spin Mn^{4+}. Hence, the Jahn-Teller effect is closely associated with high-spin Mn^{3+} and plays a vital role in in stabilizing K_xMnO_2 during electrochemical processes. Eliminating high-spin Mn^{3+} is therefore a critical factor in stabilizing K_xMnO_2.

Recently, the concept of a pseudo Jahn-Teller effect has been introduced in the context of layered oxide cathodes, resulting in asymmetric distortions of the MnO_6 octahedra. The "asymmetric MnO_6 octahedra" typically refers to Mn atoms surrounded by six oxygen (O) atoms in an octahedral arrangement where the oxygen atoms are not identical or symmetrical.[50] As a representative example, a P2-type Mn-rich cathode ($Na_{3/4}MnO_2$) has undergone meticulous examination. The MnO_6 octahedra are widely recognized for experiencing either elongation or contraction in specific directions due to the Jahn-Teller effect (JTE). In this regard, the substitution of Li for Mn ($Na_{3/4}(Li_{1/4}Mn_{3/4})O_2$) has been demonstrated to facilitate the oxidation of Mn^{3+} to Mn^{4+}, effectively suppressing the JTE. Nonetheless, the MnO_6 octahedra continue to exhibit asymmetry, with a discernible superstructural influence. Through a comprehensive array of advanced analytical techniques, Zhang et al.[51] have elucidated the pseudo-JTE as a common underlying factor for the asymmetrical distortions of the MnO_6 octahedra. These distortions have been identified as the primary cause of significant electrochemical deterioration in $Na_{3/4}Li_{1/4}Mn_{3/4}O_2$. By suppressing the pseudo-JTE, the phase transition behaviors during Na intercalation/deintercalation are modulated, thereby enhancing all electrochemical properties. The insight gained from coupling a theoretical foundation for the pseudo-JTE with empirical observations of lattice alterations in layered cathode materials suggests that many previous methodologies can be rationally explained by regulating the pseudo-JTE. This underscores the importance of considering the pseudo-JTE in the context of layered cathode materials.

In all, Jahn–Teller distortion reduces the energy of a system through specific bond length distortions, disrupting local crystal symmetry and eliminating the degeneracy of the electronic system. Among the 3d transition metal ions, high spin Mn^{3+}, high spin Fe^{4+}, and Cr^{2+} in octahedral coordination exhibit the most pronounced JT effect. Conversely, high spin Mn^{4+}, high spin Fe^{3+}, and Cr^{3+} in octahedral coordination display no Jahn–Teller effect (**Figure 3a**). Figure 3b illustrates the fundamental electronic structure instability, leading to Jahn–Teller (lattice) distortion in an octahedral ligand field, serves as the active chemical driving force for spontaneous disproportionation, phase transformation, and metal-ion dissolution in transition-metal oxides when exposed to protons. The generation of H_2O through the protonation of transition metal oxide (TMO) involves a net electron transfer originating from the TMO to the axial oxide orbital. This electron transfer is initiated by the d_z2^1 orbital of the TMO, which harbors the most reactive electron. Consequently, the protonation of the axial oxide ion and the subsequent formation of H_2O coincide with a concurrent metal-to-ligand electron transfer, resulting in an elevated oxidation state of the TM (Figure 3b). The resulting TM cations (Mn^{4+}, Fe^{5+}, and Cr^{4+}) act as potent oxidizers, reverting back to the stable, J—T free state (Mn^{2+}, Fe^{3+}, and Cr^{2+}) via a two-electron reduction pathway. This reduction process involves oxidizing electrolyte solvent molecules into CO_2 and other reactive protic species. The stable lower-valence TM oxides and fluorides exhibit a tendency to readily dissolve into the electrolyte. Simultaneously, the newly formed water molecule may react with the PF_6^- salt, generating additional HF. This establishes a closed-loop cycle, culminating in the degradation of the electrolyte salt, solvent, cathode, and anode.[30]

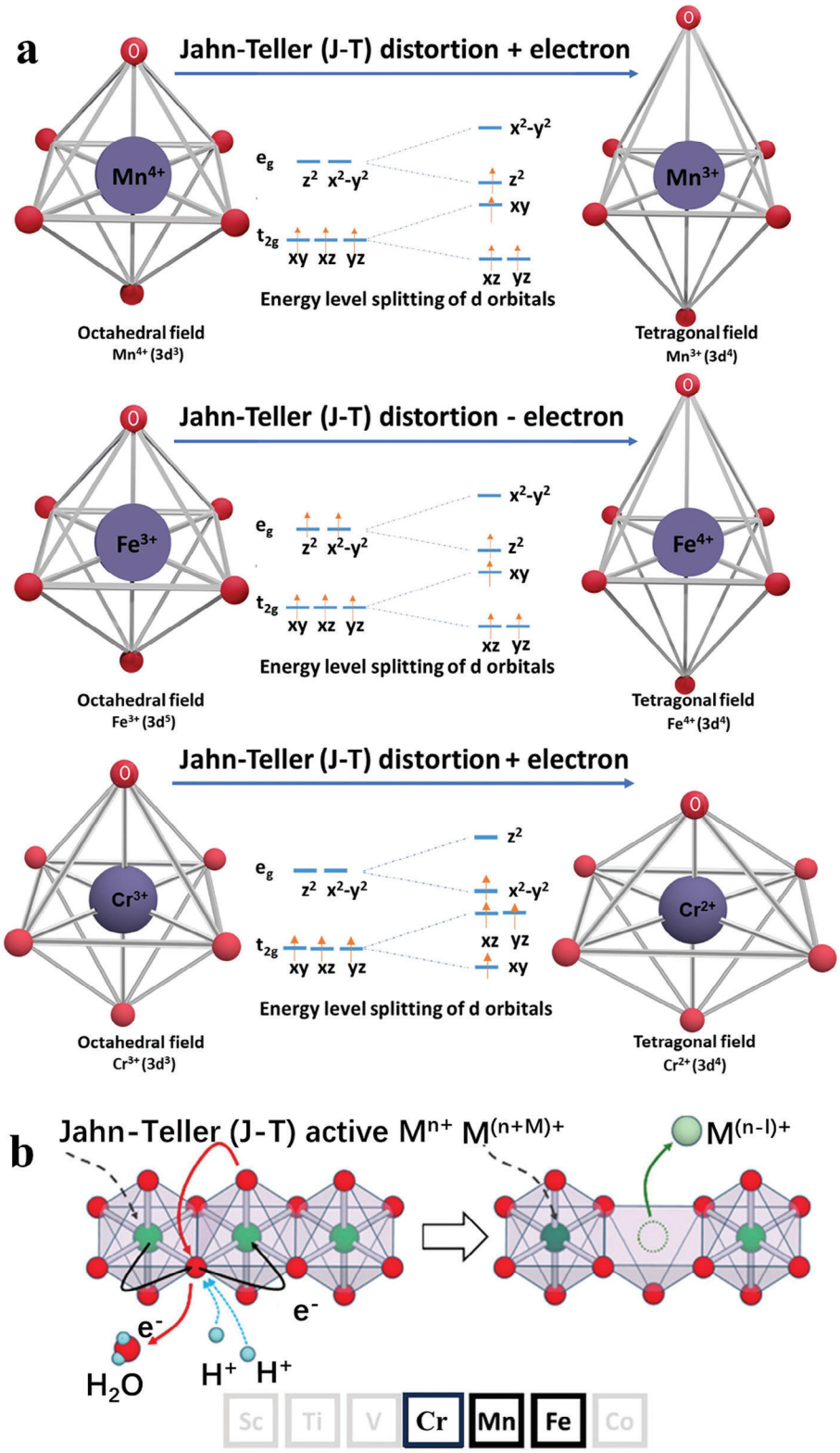

Figure 3. a) The molecular orbital energy diagram of the octahedral MO_6 and the electronic orbitals of Mn^{3+}/Mn^{4+}, Fe^{3+}/Fe^{4+}, and Cr^{2+}/Cr^{3+} ions. Reproduced with permission.[26d] Copyright 2020, AAAS: American Association for the Advancement of Science. b) Nucleophilic attack by the axial oxide on two protons (H^+) in the electrolyte transfers electrons from the d_Z2^1 orbital of the manganese to oxygen. This process forms water and causes oxidation of the M^{n+} to $M^{(n+1)+}$. Reproduced with permission.[30] Copyright 2020, American Chemical Society.

3.2. Fe Based Layered Oxides

$KFeO_2$ has emerged as a novel cathode material for PIBs. Unlike $LiFeO_2$ and $NaFeO_2$, $KFeO_2$ exhibits a unique structural characteristic with tetrahedrally coordinated Fe^{3+} ions interconnected through 3D corner-sharing.[16] Chemical oxidation of $KFeO_2$ leads to the release of ≈0.3 K^+ ions, resulting in $K_{0.7}FeO_2$, without any noticeable changes in XRD patterns. Rietveld refinement analysis of $KFeO_2$ and $K_{0.7}FeO_2$ indicates minimal variations in unit cell dimensions and the fundamental structure, while significant differences are observed in the volumes of FeO_4 tetrahedra and inter-tetrahedra angles due to the presence of Jahn-Teller active Fe^{4+} ($e_g^2t_{2g}^2$) in $K_{0.7}FeO_2$. The refinement also confirms that K^+ extraction occurs without preference from either of the two possible sites (K1 and K2), consistent with density-functional-theory calculations.

Despite the compositional and structural similarities between $KFeO_2$ and $K_{0.7}FeO_2$, the initial reversible capacity of $KFeO_2$ is measured at 60 mAh g^{-1} (≈0.28 K^+), exhibiting a plateau-like voltage response at 3.43 V versus K/K^+. In situ diffraction studies further demonstrate negligible changes in the diffraction pattern, indicating the structural stability of $KFeO_2$ and $K_{0.7}FeO_2$. However, the reversible capacity of $KFeO_2$ decreases continuously with repeated cycling, reaching 30 mAh g^{-1} after 50 charge/discharge cycles. This decay in capacity is attributed to repeated changes in the geometry of FeO_4 tetrahedra, resulting in decreased crystallinity of $KFeO_2$ and ultimately impeding facile K^+ transport. To enhance the cyclability and practicality of $KFeO_2$, future research efforts could focus on mitigating the Jahn-Teller effect, such as through isovalent doping with Al^{3+} or Ga^{3+}.[27,52] These investigations aim to address the capacity decay associated with the Jahn-Teller effect of Fe^{3+} in $KFeO_2$, thereby improving its overall performance as a cathode material for potassium-ion batteries.

3.3. Cr-Based Layered Oxides

To overcome the limitations of chromium-based layered cathode materials, particularly their limited capacity and reversibility due to the irreversible disproportionation reaction of Cr^{4+} to Cr^{3+} and Cr^{6+}, Ming[53] proposed a novel O3-type layer-structured transition metal oxide called $NaCr_{1/3}Fe_{1/3}Mn_{1/3}O_2$ (NCFM). NCFM exhibits a remarkable reversible capacity of 186 mAh g^{-1} at a current rate of 0.05C. XRD analysis reveals that NCFM undergoes a phase-transition pathway from O3 to (O3 + P3) to (P3 + O3′′) and finally back to O3′′ during the charge process. Furthermore, various spectroscopic measurements, including X-ray absorption, X-ray photoelectron, and electron energy-loss spectroscopy, provide evidence of electronic structure changes in NCFM during the deintercalation/intercalation of Na^+ ions. Experimental results confirm the effectiveness of Fe^{3+} and Mn^{4+} substitution in suppressing the disproportionation reaction of Cr^{4+} to Cr^{3+} and Cr^{6+}. These findings highlight the potential of achieving reversible multi-electron oxidation/reduction of Cr ions in NCFM, accompanied by distortion and recovery of the CrO_6 octahedra.[53] In general, octahedral sites coordinated with oxygen are occupied by Cr^{3+} and Cr^{4+} ions, while Cr^{6+} with a smaller ionic size occupies tetrahedral sites coordinated with oxygen. Bo and Ceder et al.[31] proposed that the disproportionation of Cr^{4+} is coupled with the charge transfer of three closely positioned Cr^{4+} ions, likely forming Cr^{4+} triplets, and the mobility of one Cr^{4+} ion among triplets from octahedral sites to its nearest-neighbor interstitial tetrahedral sites (Cr^{6+}). For the desodiated O3-NCFM, the distribution of Cr^{4+} in octahedral sites is homogeneous, while two-thirds of the Cr^{4+} ions in the Cr^{4+} triplets will be replaced by Mn^{4+} and Fe^{3+} ions. This substitution is activated by the uneven occupation of the t_{2g} orbitals resulting from the $t_{2g}^2\,e_g^\circ$ configuration of the Cr^{4+} ions. The Jahn-Teller effect of Cr^{4+} is confirmed by the low intensities of the Cr-O and Cr-TM peaks in the FT-EXAFS spectra, which indicate a decreased coordination number of Cr atoms after full charging. The formation of the Jahn-Teller distorted CrO_6 octahedral in the high voltage region significantly reduces the Na diffusion barrier, thereby improving Na mobility at the top of the charge.[53]

$KCrO_2$ is a unique layered compound possesses an ideal stoichiometric proportion of K^+ ions, making it highly adaptable for deployment in full cells with graphite anodes.[54] First-principle calculations carried out by Ceder[55] et al. suggest that the stabilization of layered $KCrO_2$ can be attributed to the unusual ligand field preference of Cr^{3+} toward an octahedral environment. This preference compensates for the energy penalty resulting from a shorter K^+-K^+ distance in O3–$KCrO_2$. However, the O3–$KCrO_2$ synthesized in a sealed container exhibits a significant irreversible capacity of 43 mAh g^{-1} during the first charge/discharge (C/D) cycle (135 and 92 mAh g^{-1}). This irreversible capacity is attributed to incomplete structural reversal to pristine O3 during discharge. Furthermore, $KCrO_2$ demonstrates unsatisfactory cyclic stability, with only 67% retention after 100 cycles at 10 mA g^{-1}, and poor rate capability, delivering only 31 mAh g^{-1} at 500 mA g^{-1}. Structural analysis reveals sequential phase transitions from O3 to O′3-P′3-P3-P′3-P3-O3 during charging, followed by incomplete restoration during discharge (O3–P3–P′3-P3-P′3-O′3).[55] The observed phase transitions observed in O3-$KCrO_2$ during charge and discharge were remarkably different from those of P3-$K_{0.69}CrO_2$, which was synthesized via electrochemical ion-exchange from O3-$NaCrO_2$.[56] The electrochemical method was employed as the conventional solid-state method for direct synthesis of K_xCrO_2 resulted in non-layered structures. The voltage profiles of P3-$K_{0.69}CrO_2$ also exhibited a staircase-like pattern, but only a single biphasic reaction between P3 and a faulted P3 layered structure, P″3. Although $K_{0.69}CrO_2$ required extended cycling and electrolyte replacement, which limits its commercial viability, it demonstrated significant improvement in electrochemical performance. It exhibited a capacity retention of 65% after 1000 charge/discharge cycles and a rate performance of 65 mAh g^{-1} at 1 A g^{-1}. The distinct differences between O3-$KCrO_2$ and P3-$K_{0.69}CrO_2$ suggest that the initial state of K_xCrO_2 can influence both the phase evolution during charge/discharge and the resulting electrochemical properties.[57] Currently, there is a dearth of practical investigations on the Jahn-Teller effect induced by Cr^{4+} in $KCrO_2$, and in fact it is Cr^{2+} that induces the strong Jahn-Teller distortion. Therefore, future research on Cr-based materials for application in PIBs should explore this aspect.

The presence of Mn^{3+} as a Jahn-Teller active ion results in local distortion or cooperative lattice distortion. In O3 and P2 type frameworks, the combination of the low redox potential of $Mn^{3+/4+}$ and high Mn^{3+} content can induce structural

Table 1. Summary of properties and functions of metal elements in K^+ layer oxide cathodes.[18,58]

Element	Element abundance (ppm)	Cathode material	Common oxidation state in layered oxides (spin state)	Electron configuration in layered oxides	Jahn–Teller distortion	Disadvantage	References
Mn	950	P3-$K_{0.45}MnO_2$	+3(HS)/+4	[Ar]$3d^4$ (t_{2g}^3 e_g^1)/ [Ar]$3d^3$ (t_{2g}^3 e_g^0)	Strong/-	J-T effect active Mn^{3+}	[48]
Fe	56 300	P2-$K_{0.65}Fe_{0.5}Mn_{0.5}O_2$	+3(HS)/+4(HS)	[Ar]$3d^5$ (t_{2g}^3 e_g^2)/ [Ar]$3d^4$ (t_{2g}^3 e_g^1)	-/Strong	J-T active Fe^{4+}	[7,18]
Cr	102	O3-$KCrO_2$	+3	[Ar]$3d^3$ (t_{2g}^3 e_g^0)	_	Phase transitions, Toxic, complex	[55]

deformation and deterioration of electrochemical properties. Doping with Fe^{3+} introduces a Jahn-Teller active ion of Fe^{4+} which provide the buckling capability to reduce the migration barrier during charging, which enhances K ions diffusion and extraction.[31] In addition, Cao's study[53] confirms the Jahn-Teller effect of Cr^{4+} through the observed low intensities of the Cr-O and Cr-TM peaks in the FT-EXAFS spectra. The formation of Jahn-Teller distorted CrO_6 octahedra in the high voltage region significantly reduces the Na diffusion barrier. Further research on potassium-ion-based systems such as $KCrO_2$ is limited, and additional theoretical and experimental studies in this area anticipated in the future. Overall, the Jahn-Teller distortion of MO_6 octahedra in K_xMO_2 (M = Mn, Fe, Cr) can result in severe structural instability and degradation during electrochemical cycling, presenting challenges for practical applications. Therefore, the development of advanced material design strategies that effectively eliminate the Jahn-Teller effect is highly anticipated to enable K_xMO_2 (M = Mn, Fe, Cr) to be a commercially viable cathode material for PIBs. The properties and functions of metal elements in K^+ layer oxide cathodes are summarized in **Table 1**.

4. The Way to Suppress the Jahn-Teller Effect

To mitigate the challenges posed by Jahn-Teller effect, numerous design strategies have been devised to enhance the electrochemical performance of these materials. These strategies encompass elemental doping, surface coating, and diverse synthesis strategies[24] (**Figure 4**). As Mn-based layered metal oxides are among the extensively investigated materials in this category, our strategic focus revolves around resolving the structural deformation resulting from the Jahn-Teller effect within these compounds.

4.1. Element Doping

Three distinct types of dopants, transition metal (TM), potassium (K), and oxygen (O), can be identified based on the substitution/doping sites. In the study conducted by Zheng et al.,[60] they elucidate the substitution of a proportion of the Mn element with Zn, serving as an exemplification of TM site doping. Lu et al.[61] present evidence of K site doping by replacing a segment of the K element with Rb. Furthermore, Wan et al.[62] exemplifies O site doping by showcasing the substitution of a fraction of the O element with F. The substitution of elements, which can be easily accomplished using common preparation methods, offers a promising approach to regulate the properties of cathode materials. Consequently, this strategy serves as a simple and effective means to potentially optimize the performance of the cathode material for PIB.[20] **Table 2** provides an overview of the roles played by different elements in the doping of K_xMnO_2.

4.1.1. Substitutions at TM Sites

Various popular dopants, such as Ni, Co, Fe, Al, Ti, Mg, and Cr, have been utilized at TM sites to modify the atomic structures of neighboring Mn ions, resulting in more stable average structures compared to pristine materials. These dopants also aid in adjusting the valence of Mn to levels above 3.5+, thus avoiding the occurrence of violent Jahn-Teller regions. For instance, Yun-Sung Lee et al. fabricated a P3-type binary oxide, $K_{0.45}Mn_{0.5}Co_{0.5}O_2$, by introducing Co as a dopant. This electrode material exhibited a specific capacity of 140 mAh g^{-1}, involving both Mn^{3+}/Mn^{4+} and Co^{3+}/Co^{4+} redox couples. During the charging process, the extraction of K^+ ions led to the oxidation of Mn^{3+} to Mn^{4+} at low voltage and the oxidation of Co^{3+} to Co^{4+} at high voltage. It is noteworthy that the Jahn-Teller distortion induced by Mn^{3+} can unidirectionally increase the Mn—O distance in discharged Mn-based cathode materials.[63] In a study by Zhang et al., they synthesized a 5% Co-doped Mn-based layered oxide ($K_{0.3}Mn_{0.95}Co_{0.05}O_2$) with excellent cycling capability, demonstrating a capacity retention of 75% after 500 cycles. The successful doping of Co effectively suppressed the Jahn-Teller effect, leading to more isotropic K^+ migration pathways and ultimately improving ionic diffusion and cycling stability.[64] Choi[5]proposed P3-$K_{0.54}[Co_{0.5}Mn_{0.5}]O_2$ as a cathode material designed to enhance the performance of PIBs. The composition design focus on utilizing the valence state of Mn above 3.5+ to minimize the disruptive effect of Jahn-Teller distortion in the MnO_6 octahedra during the electrochemical reaction. Unlike other layered materials that experience sluggish diffusion of large potassium ions, resulting in multi-step voltage profiles, P3-$K_{0.54}[Co_{0.5}Mn_{0.5}]O_2$ offers a high specific discharge capacity of 120.4 mAh (g-oxide)$^{-1}$, accompanied by smooth charge and discharge curves. Moreover, even at 500 mA g^{-1}, P3-$K_{0.54}[Co_{0.5}Mn_{0.5}]O_2$ maintains a high discharge capacity of 78 mAh g^{-1}, equivalent to 65% of the capacity obtained at 20 mA g^{-1}. This demonstrates the significant potential of P3-$K_{0.54}[Co_{0.5}Mn_{0.5}]O_2$ as a high-performance cathode material for PIBs.[19] In another study, $K_{0.48}Mn_{0.4}Co_{0.6}O_2$, a P3-type layered oxide, was synthesized using a solid-state method and stabilized in a rhombohedral structure [space group R3m (#160)]. This cathode material exhibited a reversible capacity of 64 mAh g^{-1} at 3.0 V (vs K/K^+), along with good cycling stability. After 180 cycles, the cathode maintained stable cycling and good capacity retention,

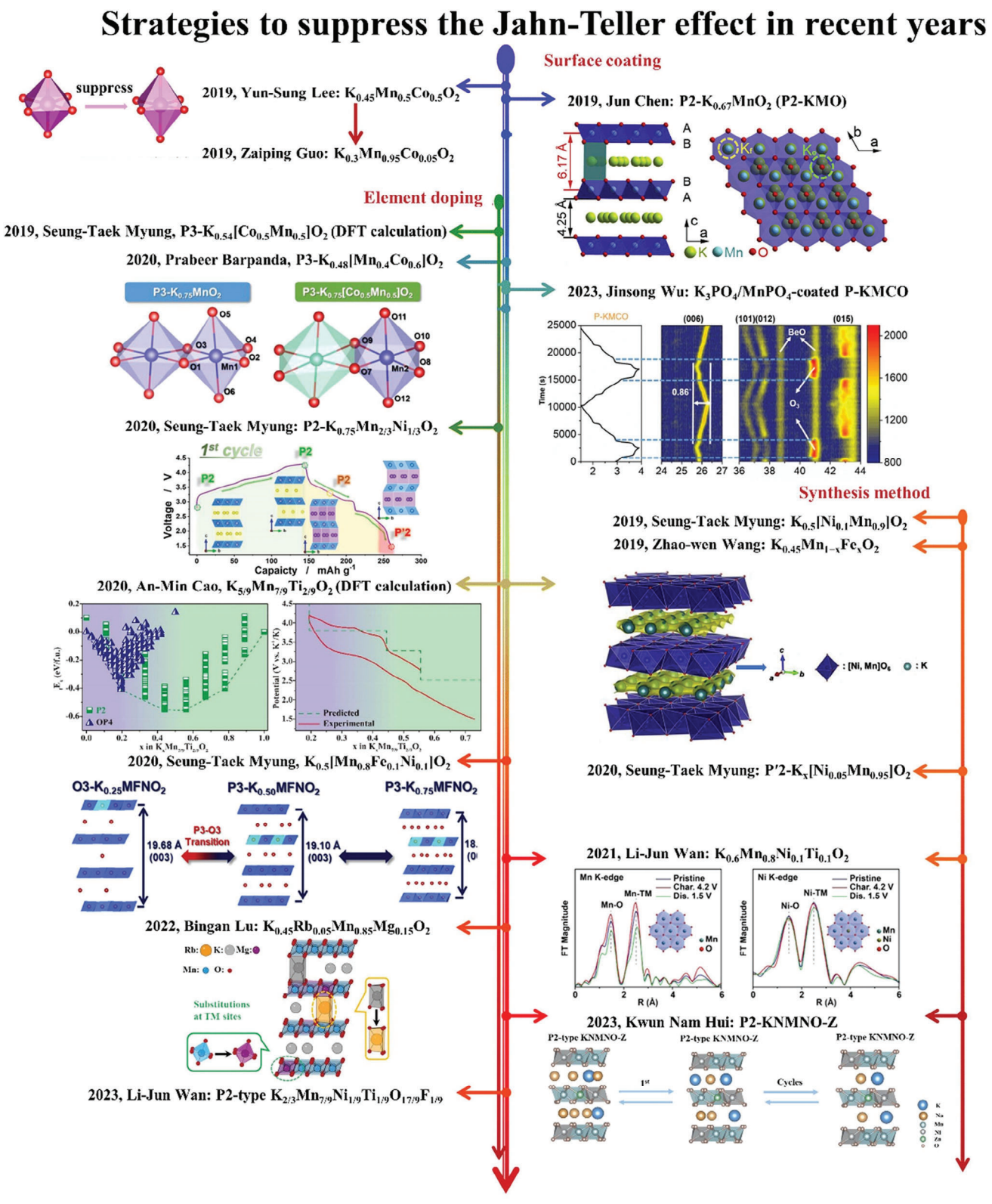

Figure 4. Schematic illustrations of synthesis strategies of K_xMO_2 for the suppression of the Jahn-Teller effect. These literature statistics are presented in Table 4.

Table 2. Summary of the role of doping elements.

Elements	Advantages	Doping site	References
Co	Suppressed J-T effect, enhancing K^+ migration and cycling stability with isotropic pathways.	TM	[63]
Ni	Stabilize structure by minimizing Mn^{3+} and mitigating J-T effect for suppressing lattice shrinkage and expansion.	TM	[67]
Fe	Induce structural modifications in neighboring manganese ions, resulting in the formation of a more stable atomic configuration	TM	[70]
Mg	Mitigates J-T distortions, increases interlayer spacing, promotes K^+ diffusion	TM	[71]
Ti	An inactive element, increased the covalency of Mn—O bonds and mitigated the volume change of the material	TM	[75]
Al	Al^{3+} enhances interlayer spacing in K^+ layer without charge compensation.	TM	[80]
Rb	Uniformly adjust bond lengths in K layer to preserve MnO_6 octahedra symmetry.	K	[60]
F	F^- enhances interlayer spacing, facilitating K^+ (de)intercalation and preventing structural degradation. It suppresses oxygen loss linked to oxygen redox.	O	[61]

with 81% of the initial capacity remaining.[65] In conclusion, the effective cobalt doping strategy showcased its ability to mitigate the detrimental impact of Jahn-Teller distortion in the MnO_6 octahedra during the electrochemical reaction, leading to improved ion diffusion and enhanced cycling stability.

The incorporation of Ni has proven to be an effective approach in mitigating Jahn-Teller distortion and enhancing the structural stability of the material, resulting in improved stability performance. Both theoretical and experimental investigations have demonstrated that P2-$K_{0.75}[Ni_{1/3}Mn_{2/3}]O_2$ undergoes a single-phase reaction involving a Ni^{4+}/Ni^{2+} redox couple, while Mn^{4+} remains inactive during the charge/discharge operations within the operational range. Remarkably, P2-$K_{0.75}[Ni_{1/3}Mn_{2/3}]O_2$ has exhibited a discharge capacity of 91 mAh g^{-1} and outstanding cycling stability, with 83% capacity retention after 500 cycles at 1400 mA g^{-1}.[65] In another study by Choi et al.[66] P'2-$K_{0.83}[Ni_{0.05}Mn_{0.95}]O_2$ was synthesized, demonstrating remarkable cyclic stability by retaining the P′2 phase without transitioning to OP4 during K^+ extraction/insertion. First-principles calculations revealed a low activation energy barrier of 271 meV, facilitating efficient K^+ diffusion in P'2-$K_{0.83}[Ni_{0.05}Mn_{0.95}]O_2$ and enabling its high power capability. Additionally, Cho et al.[67] introduced a new cathode material, P3-$K_{0.5}[Ni_{0.1}Mn_{0.9}]O_2$, by incorporating a small amount of divalent Ni, resulting in an impressive initial discharge capacity of 121 mAh g^{-1} at a current of 10 mA g^{-1} and retaining 82% of its capacity after 100 cycles. The introduction of Ni has been shown to enhance the stability of the material structure by reducing the proportion of Mn^{3+} and mitigating the Jahn-Teller effect, thereby suppressing lattice shrinkage and expansion. Similarly, Bai et al.[68] proposed a new cathode material, P3-$K_{0.67}Ni_{0.17}Mn_{0.83}O_2$, which demonstrated an impressive specific capacity of 122 mAh g^{-1} at 20 mA g^{-1}. The material exhibited good cycling stability, retaining 75% of its capacity at 500 mA g^{-1} after 200 cycles. It was found that this material exhibited a larger K^+ ion diffusion coefficient (10^{-13} to 10^{-11} cm^2 s^{-1}) compared to the Ni-free electrode (10^{-15} to 10^{-11} cm^2 s^{-1}), indicating improved ion transport properties. In a study by Zhang et al.,[2] a P2-type cathode material, $K_{0.44}Ni_{0.22}Mn_{0.78}O_2$, was synthesized using a solid-state method. This cathode material delivered a specific capacity of 125.5 mAh g^{-1} at 10 mA g^{-1} and retained 67% of its initial capacity after 500 cycles at 200 mA g^{-1}. Importantly, it was observed that trace amounts of NiO impurities in the as-synthesized material were electrochemically inactive during charging and discharging (**Figure 5**a,b). The XRD pattern of $K_{0.44}Ni_{0.22}Mn_{0.78}O_2$ at the open circuit voltage (OCV) is nearly identical to the pristine material, except for the presence of NiO and Al foil peaks. This suggests that $K_{0.44}Ni_{0.22}Mn_{0.78}O_2$ undergoes solid-solution processes without significant phase transitions. During K^+ extraction, the (002) and (004) peaks shift to lower angles, while the (010) and (012) reflections shift to higher angles, indicating c-axis expansion and ab plane contraction due to electrostatic repulsion and ionic radius changes. Importantly, these peak shifts are reversible when K^+ is reinserted into the crystal lattice. In situ XRD patterns revealed a single-phase transition and a small volumetric change of 1.5% upon K^+-ion extraction/insertion (Figure 5c). The authors also noted that the partial substitution of Ni^{2+} for Mn^{3+} in P3-K_xMnO_2 effectively mitigated the structural deterioration caused by the Mn^{3+}-ion-induced Jahn-Teller effect, leading to improved structural stability and higher reversible capacity. In another study by Duan et al.,[69] the P3-type cathode material, $K_{0.5}Mn_{0.7}Ni_{0.3}O_2$ (KMNO), was reported to exhibit exceptional rate capability, delivering a capacity of 57.1 mAh g^{-1} at 500 mA g^{-1}. The material also demonstrated remarkable cycling stability, retaining 77.0% of its capacity after 300 cycles at 100 mA g^{-1}. The authors attributed these superior properties to the presence of Ni, which not only stabilizes the structure by alleviating Jahn-Teller distortion and suppressing phase transitions, but also contributed to the material's capacity as an electrochemically active element, allowing the transition of two electrons from Ni^{2+} to Ni^{4+}. To summarize, partial substitution of Ni^{2+} for the Jahn-Teller active Mn^{3+} has been effective in mitigating P2-O2 phase transitions and structural degradation in Mn/Ni-based compounds. Furthermore, the utilization of the $Ni^{2+/4+}$ redox couple has demonstrated a high average voltage, which is advantageous for the development of high-energy density batteries.[18]

The introduction of Fe doping has been shown to induce structural modifications in neighboring manganese ions, resulting in the formation of a more stable atomic configuration and leading to enhanced cycling performance. In a study by Deng et al.,[7] P2-type $K_{0.65}Fe_{0.5}Mn_{0.5}O_2$ (P2-KFMO) microspheres were designed using a modified solvent-thermal method. These microspheres,

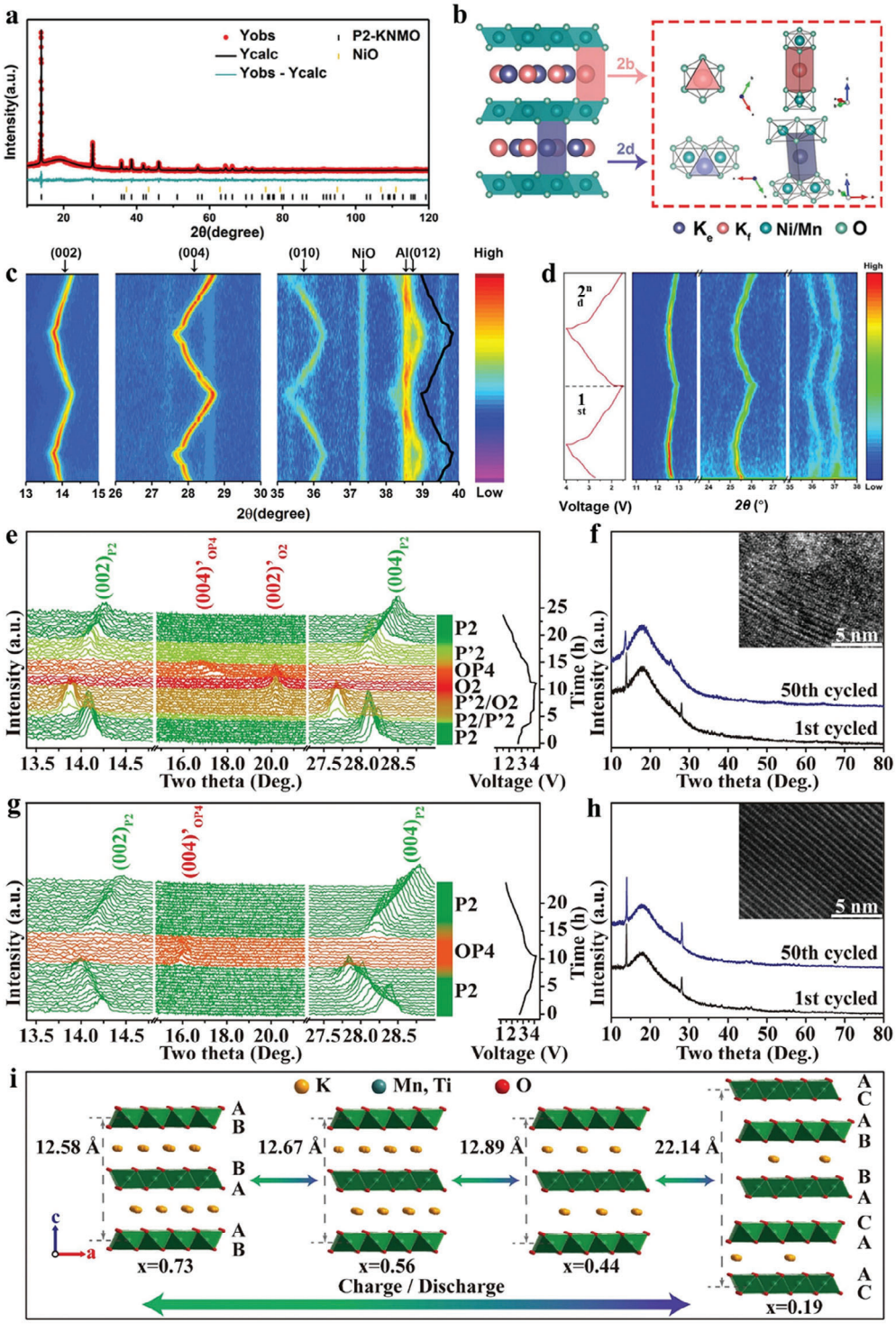

Figure 5. a) XRD Rietveld refinement of $K_{0.44}Ni_{0.22}Mn_{0.78}O_2$ material. Reproduced with permission.[2] Copyright 2019, Wiley-VCH. b) Schematic illustration of the hexagonal $K_{0.44}Ni_{0.22}Mn_{0.78}O_2$ obtained from Rietveld refinement of XRD data. Reproduced with permission.[2] Copyright 2019, Wiley-VCH. c) 2D plot of in situ XRD patterns of $K_{0.44}Ni_{0.22}Mn_{0.78}O_2$ electrode collected during the first and second charge/discharge at 10 mA g^{-1} in the voltage range of 1.5–4.0 V. Reproduced with permission.[2] Copyright 2019, Wiley-VCH. d) 2D plot of in situ XRD patterns of $K_{0.54}Mn_{0.78}Mg_{0.22}O_2$ during the first two cycles. Reproduced with permission.[72] Copyright 2021, Tsinghua Univ Press. Structure evolution of the P2-type KMTO-x upon K^+ insertion/extraction. e,f) In situ XRD patterns and corresponding voltage–capacity curve of P2-type KMTO-0 and P2-type KMTO-2/9 at current rate 10 mA g^{-1}, respectively, g,h) X-ray diffraction patterns of the P2-type KMTO-0 and P2-type KMTO-2/9 samples after different cycles, respectively, i) Schematic illustration showing the P2-OP4 phase evolution mechanism of KMTO-2/9 upon the K^+ insertion/extraction. e-i) Reproduced with permission.[74] Copyright 2020, Elsevier.

composed of primary nanoparticles, exhibited improved K^+ intercalation/deintercalation kinetics due to the stabilized cathodic electrolyte interphase on the cathode. The P2-KFMO microspheres demonstrated a highly reversible potassium storage capacity of 151 mAh g^{-1} at 20 mA g^{-1}, fast rate capability of 103 mAh g^{-1} at 100 mA g^{-1}, and long-term cycling stability, retaining 78% of its capacity after 350 cycles. Furthermore, an interconnected nanowire skeleton structure of $K_{0.7}Fe_{0.5}Mn_{0.5}O_2$ was synthesized for the first time, exhibiting an ultra-high initial discharge capacity of 178 mAh g^{-1} at 20 mA g^{-1}.[46] The unique nanowire morphology led to exceptional cycling stability, with the material retaining 87% of its capacity at 500 mA g^{-1} after 200 cycles. The 3D network structure provided channels for both K^+ diffusion and electron transmission. In a systematic investigation conducted by Liu et al.[70] various samples of $K_{0.45}Mn_{1-x}Fe_xO_2$ were studied, and it was found that $K_{0.45}Mn_{0.8}Fe_{0.2}O_2$ exhibited the best cyclic stability and rate performance. This composition demonstrated a significant reversible discharge capacity of 106.2 mAh g^{-1} at 20 mA g^{-1}, with a capacity retention rate of 77.3% after 100 cycles. The results indicate that even a relatively small substitution (20%) at the transition metal site can improve the cycle stability during potassium ion insertion and extraction. Furthermore, Masese et al.[27] synthesized a unique layered oxide cathode, $K_{0.4}Fe_{0.5}Mn_{0.5}O_2$, which sets itself apart from other Fe/Mn-based layered oxides that typically contain trivalent Fe^{3+} and Mn^{3+}. This cathode material exhibited a reversible specific capacity of 120 mAh g^{-1} and an average discharge voltage of 2.8 V. In summary, the incorporation of Fe metal into the K_xMnO_2 system has been shown to enhance the specific capacity and average voltage corresponding to the $Fe^{3+/4+}$ redox couple. From a practical perspective, Mn/Fe-based electrodes are attractive for energy storage applications due to the abundance, cost-effective, and non-toxic nature of these elements. However, it is crucial to address the Jahn-Teller effect associated with Mn^{3+} and Fe^{4+} ions, and further research is necessary to optimize these materials for long-lasting battery performance.

The incorporation of electrochemically inactive elements (such as Mg^{2+} and Ti^{4+}) through doping proven to be an effective strategy in mitigating the structural deterioration caused by the Jahn-Teller effect of Mn^{3+} and significantly enhancing the long-term cycling performance of layered oxides. In a study by Liu et al.,[71] layered P3 type $K_{0.45}Mn_{0.9}Mg0_{.1}O_2$ was successfully synthesized using a facile solid-state reaction process. The electrochemical performance of $K_{0.45}Mn_{0.9}Mg0_{.1}O_2$ was thoroughly investigated, revealing a high reversible capacity of 108 mAh g^{-1} at 20 mA g^{-1}, attributed to the beneficial effect of Mg substitution on cyclability. Even after 100 cycles, $K_{0.45}Mn_{0.9}Mg0_{.1}O_2$ retained a capacity of ≈80.8 mAh g^{-1} at 20 mA g^{-1} and demonstrated outstanding rate capability of 69.8 mAh g^{-1} even at 200 mA g^{-1}. Importantly, the structural integrity of the original $K_{0.45}MnO_2$ was preserved following Mg substitution, indicating that the Jahn-Teller effect can be mitigated by low-valence Mg^{2+} substitution for Mn^{3+}. The incorporation of small amounts of Mg has been shown to be an effective compensation mechanism in enhancing the capacity and stability of the material. In a recent study by Huang et al.,[72] they reported a novel Mn-based layered oxide, $K_{0.54}Mn_{0.78}Mg_{0.22}O_2$, which exhibited exceptional electrochemical performance characteristics, including high specific capacity and excellent high-rate cycling stability. The solid-solution process during the initial two cycles is more evident when examining the 2D plot presented in Figure 5d. This analysis further confirms that $K_{0.54}Mn_{0.78}Mg_{0.22}O_2$ can consistently facilitate structural evolution and achieve a complete single-phase transition. These findings strongly suggest that the doping of inactive Mg^{2+} species can effectively mitigate the adverse Jahn-Teller effect, thereby facilitating the remarkable stability of the material's structural configuration (Figure 5d). Leveraging the unique layered structure and an effective Mg doping strategy, $K_{0.7}Mn_{0.7}Mg_{0.3}O_2$ particles have demonstrated remarkable electrochemical properties. The material exhibits a high reversible capacity of 144.5 mAh g^{-1} at 20 mA g^{-1}, accompanied by an excellent capacity retention rate of 82.5% after 400 cycles.[73] Similarly, in the case of $K_{5/9}Mn_{7/9}Ti_{2/9}O_2$, where Mn^{4+} is partially replaced with Ti^{4+}, a stable P2-OP4 phase transition has been observed (Figure 5e,f). The presence of Ti^{4+} with a similar valence state and ionic radius close to that of Mn^{4+} (0.605 vs 0.53 Å) counteracts the gliding tendency of MnO_6 slabs during electrochemical processes. As a result, it enables a highly reversible P2-OP4 phase transition, as opposed to the P2–O2 and O3–P3 transitions. In addition, the OP4 phase proved to be non-destructive compared to the heavily-deformed O2 phase and could reversibly transition back to the P2 structure, as confirmed by XRD and high-resolution transmission electron microscopy (HRTEM) analysis of cycled samples (Figure 5g,h). Notably, no significant structural deformation was observed in the P2-type KMTO-2/9 sample even after 50 cycles. Figure 5i illustrates the lattice structures at different charge/discharge stages of K_xMTO-2/9. These structures underwent minor alterations in lattice spacings in response to changes in K^+ content and displayed remarkable reversibility over extended cycles.[74] Thus, the inhibition of Jahn-Teller has a stabilizing effect on the structure evolutions of materials at atomic-scale during cycling. Zhang et al.[75] successfully synthesized a cost-effective P3-type cathode material, P3-$K_{0.4}Fe_{0.1}Mn_{0.8}Ti_{0.1}O_2$, through the substitution of Mn with both Fe and Ti. This material exhibited exceptional electrochemical performance, with a discharge capacity of 117 mAh g^{-1} at 20 mA g^{-1} and a high-rate capability of 71 mAh g^{-1} at 1000 mA g^{-1}. The remarkable discharge capacity was attributed to the synergistic effect of doped Fe, Ti, and Mn. The Fe^{3+}/Fe^{4+} redox couple displayed a high redox potential, effectively reducing the diffusion barrier for K^+ ions. The presence of Ti, as an inactive element, increased the covalency of Mn—O and Fe—O bonds and mitigated the volume change of the material, thus stabilizing the crystal structure and maintaining capacity stability. In a separate study by Xu,[76] a P2-type cathode, $K_{0.6}Mn_{0.8}Ni_{0.1}Ti_{0.1}O_2$ (KMNT), was developed and demonstrated to possess a highly reversible K^+ (de)intercalation capability up to 4.2 V. KMNT exhibited an improved long-term cycling capability, with a capacity retention rate of 88% after 100 cycles at 200 mA g^{-1}, in contrast to KMO, which had a capacity retention rate of 59%. These results indicate that the presence of Ni and Ti effectively suppressed the structural damage related to the Jahn-Teller effect of Mn^{3+} and mitigated the detrimental lattice sliding of transition metal layers at high voltage.

To summarize, the doping electrochemically inactive elements (such as $Mg^{2+}$and Ti^{4+}) offers a valuable strategy for suppressing structural transitions and improving the long-term cyclability of layered compounds. The incorporation of Mg^{2+} effectively mitigates Jahn-Teller distortions, increases interlayer spacing,

promotes K^+ diffusion and enhances the rate capability. On the other hand, Ti^{4+} substitution hinders layer gliding and enhances structural stability during charge/discharge processes. It is important to note that excessive doping of inactive elements can result in a decrease in specific capacity, highlighting the need for careful optimization of dopant concentrations when designing efficient electrode materials.[18]

Extensive research has been focused on the incorporation of dual dopants at the Mn site in cathode materials for PIBs. Several dopants, including Ni, Co, Fe, Ti, Mg, and Al, have been investigated to enhance the electrochemical performance of K_xMnO_2 compounds. In 2017, Liu[78] et al. reported a ternary material, $K_{0.67}Ni_{0.17}Co_{0.17}Mn_{0.66}O_2$, and explored the influence of preparation conditions on the material's morphology. The material exhibited an initial discharge capacity of 77 mAh g^{-1}, after 100 cycles, it retained 87% of its capacity. Furthermore, Xu[79] et al. reported a layered cathode material, $K_{0.48}Ni_{0.2}Co_{0.2}Mn_{0.6}O_2$ (KNCMO), which exhibited a unique morphology of microspheres and microcubes. When evaluated as a cathode in PIBs, KNCMO demonstrated remarkable electrochemical properties, delivering a reversible capacity of ≈57 mAh g^{-1} at 40 mA g^{-1} and exhibiting good rate performance. Furthermore, even at 400 mA g^{-1}, the KNCMO maintained a considerable reversible capacity of ≈35 mAh g^{-1} after 350 cycles. The use of P3-$K_{0.5}Mn_{0.72}Ni_{0.15}Co_{0.13}O_2$ microspheres as cathodes demonstrated superior electrochemical performance, with an initial discharge capacity of 82.5 mAh g^{-1} and remarkable cycling stability. After 100 cycles at 50 mA g^{-1}, it retained 85% of its capacity.[80] In a separate study, Dang et al.[81] enhanced the electrochemical performance of P3-$K_{0.45}Ni_{0.1}Co_{0.1}Mn_{0.8}O_2$ by introducing Mg^{2+} and Al^{3+} dopants at Mn sites. The Mg^{2+}/Al^{3+} doping led to an increase in the interlayer spacing of the K^+ layers, potentially reducing the resistance to K^+ migration during cycling. Although the doped samples exhibited reduced discharge capacities compared to the pristine sample, attributed to the decreased $Mn^{3+/4+}$ active redox content as Mg^{2+}/Al^{3+} did not participate in charge compensation, the Mg^{2+} and Al^{3+} doping improved the cathode's cycling stability. This was achieved by mitigating the Mn^{3+}-induced Jahn-Teller distortion, expanding the K^+-ion diffusion layer, and reinforcing the cathode's structural stability (**Figure 6a–c**).

Researchers have explored the co-doping of Ni and Fe as a means to alleviate the Jahn-Teller effect. Hwang et al.[82] synthesized P2-$K_{0.75}[Mn_{0.8}Ni_{0.1}Fe_{0.1}]O_2$ through electrochemical ion exchange, resulting in cathode that exhibited reversible storage of K^+-ions (0.5 mol). This enabled a capacity of 110 mAh g^{-1} without undergoing multiple phase transitions within 1.5–3.9 V. Furthermore, the P2-$K_{0.75}[Mn_{0.8}Ni_{0.1}Fe_{0.1}]O_2$/hard carbon full cell demonstrated remarkable long-term stability over 1000 consecutive cycles. In a study by Choi et al.,[83] P3-$K_{0.5}[Mn_{0.8}Fe_{0.1}Ni_{0.1}]O_2$,was synthesized using a combustion-assisted solid-state reaction. The substitution of Fe^{3+} and Ni^{2+} for Mn^{3+} elevated the average Mn valence state to 3.75+, effectively mitigating Jahn-Teller distortions and structural degradation (Figure 6d–f). Operando synchrotron XRD (O-SXRD) analysis was conducted to examine the structural changes in P3-type $K_{0.5}[Mn_{0.8}Fe_{0.1}Ni_{0.1}]O_2$ during K^+ de/intercalation. The XRD patterns revealed that during charging, certain P3 peaks shifted toward lower angles, while others gradually shifted toward higher angles. A phase transition from P3 to the O3 phase occurred between 3.5 and 3.9 V, as indicated by the appearance of the (104) peak of the O3 phase. Notably, the P3 (105) peak was absent, suggesting the absence of a phase transition to the "X" phase observed in $K_x[Mn_{0.8}Fe_{0.1}Ni_{0.1}]O_2$ (x = 0.25–0.34). This absence of a phase transition to the "X" phase was attributed to the substitution of Mn^{3+} with Fe and Ni in $K_{0.5}[Mn_{0.8}Fe_{0.1}Ni_{0.1}]O_2$ (Figure 6g,h). Despite a slight change in reversibility (≈4.1%), the P3-$K_{0.5}[Mn_{0.8}Fe_{0.1}Ni_{0.1}]O_2$ cathode achieved a high discharge capacity of 120 mAh g^{-1} and maintained 74% of its initial capacity after 300 cycles

Furthermore, the development of Mg–Ni co-substituted $K_{1/2}Mn_{5/6}Mg_{1/12}Ni_{1/12}O_2$, referred to as KMMN-2, as a promising cathode material for PIBs has been reported.[84] This material demonstrates suppressed phase transitions observed in $K_{1/2}MnO_2$ and improved K^+ storage performance. The incorporation of Mg^{2+} and Ni^2 into the K^+ layer acts as a "nailed pillar" that hinders the gliding of the metal oxide layer during K^+ (de)intercalation. The "Mg–Ni pinning effect" not only suppresses phase transitions but also reduces volume variation, thereby improving cycle performance. Cycling profiles reveal that KMMN-2 outperforms KMO in terms of both reversible capacities and cyclic stability. KMMN-2 achieves an initial capacity of 83.3 mAh g^{-1} with 70.4% capacity retention after 200 cycles, while KMO delivers 71.7 mAh g^{-1} with only 51.9% capacity retention at 120 mA g^{-1}.

The ternary doping strategy mentioned above represents a pioneering development direction for cathode materials used in PIBs, making a significant breakthrough in the field. These studies demonstrate that the substitution of metal elements, such as Ni, Co, Fe, Ti, Mg, and Al, in layered K_xMnO_2 effectively suppresses Jahn-Teller distortions and structural changes during K^+ deintercalation/intercalation. In general, the introduction of Mg^{2+} and Al^{3+} doping enhances the cycling stability of the cathode by mitigating the Jahn-Teller distortion induced by Mn^{3+}, expanding the diffusion layer for K^+ ions, and improving the structural integrity of the cathode. On the other hand, the substitution of Mn^{3+} with Fe^{3+} and Ni^{2+} increases the average valence of Mn to 3.75+, effectively alleviating the Jahn-Teller distortion and structural degradation. Additionally, the incorporation of Mg^{2+} and Ni^{2+} into the K^+ layer serves to suppress phase transitions and reduce volume changes, thereby enhancing the cycling performance of the cathode.[18]

4.1.2. Substitutions at K Sites

The incorporation of dopants such as Na, Rb, and Ti[9,60,85] into the K sites of layered materials has shown potential to enhance their structural stability. These dopants, especially the larger ones, can adjust the bond lengths uniformly within the K layer, thereby preserving the symmetry of MnO_6 octahedra. Lu et al.[61] introduced a P3-type $K_{0.45}Rb_{0.05}Mn_{0.85}Mg_{0.15}O_2$ (KRMMO) cathode material as a promising candidate for PIBs. Their investigation demonstrates that Rb acts as a stabilizing agent, expanding the interlayer spacing and enhancing the structural stability. Furthermore, the partial substitution of Mn with Mg effectively mitigates the Jahn-Teller distortion of Mn^{3+} ions. In situ XRD and XPS analysis confirm that KRMMO maintains its P3 phase structure during K^+ extraction/insertion, indicating excellent phase

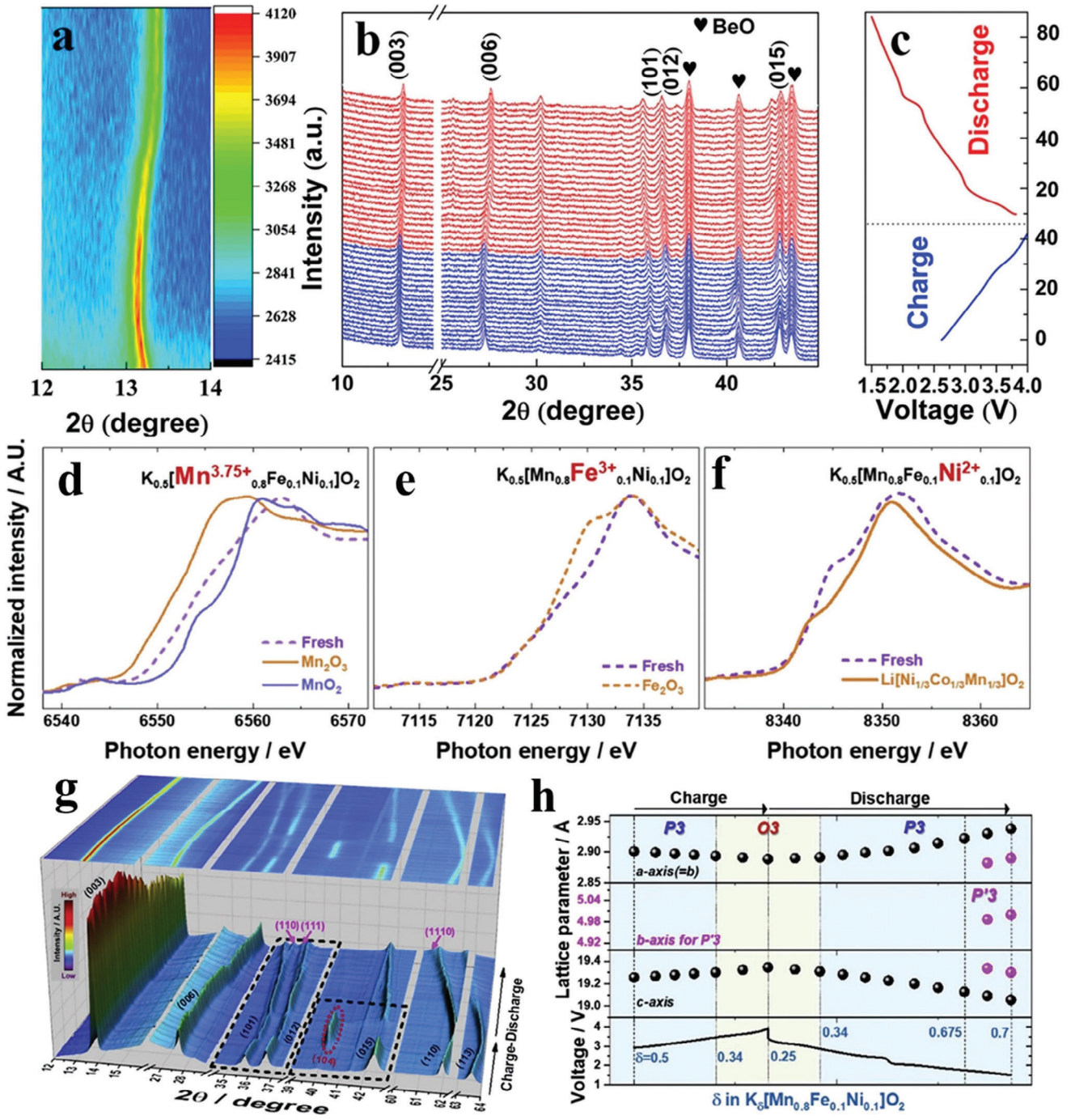

Figure 6. In situ XRD patterns collected at initial cycling. a) The image plots of the in situ XRD peaks for the peak of (003). b) In situ XRD patterns collected during the first charge and discharge processes at 10°–45° and c) the first cycle charge/discharge profiles under a current density of 10 mA g^{-1} within the voltage range of 1.5–4.0 V for Al-doped. a–c) Reproduced with permission.[80] Copyright 2020, Elsevier. Ex situ XANES spectra for the d) Mn K-edge, e) Fe K-edge, and f) Ni K-edge of the P3-type $K_{0.5}[Mn_{0.8}Fe_{0.1}Ni_{0.1}]O_2$ fresh powder.[82] g) Operando SXRD patterns for the P3-type $K_{0.5}[Mn_{0.8}Fe_{0.1}Ni_{0.1}]O_2$ electrode with Kapton film: 17°–30°.[82] h) The lattice parameters calculated from operando XRD patterns from $K_{0.25}[Mn_{0.8}Fe_{0.1}Ni_{0.1}]O_2$ to $K_{0.7}[Mn_{0.8}Fe_{0.1}Ni_{0.1}]O_2$ during the charge–discharge processes. d-h) Reproduced with permission.[82] Copyright 2020, Elsevier.

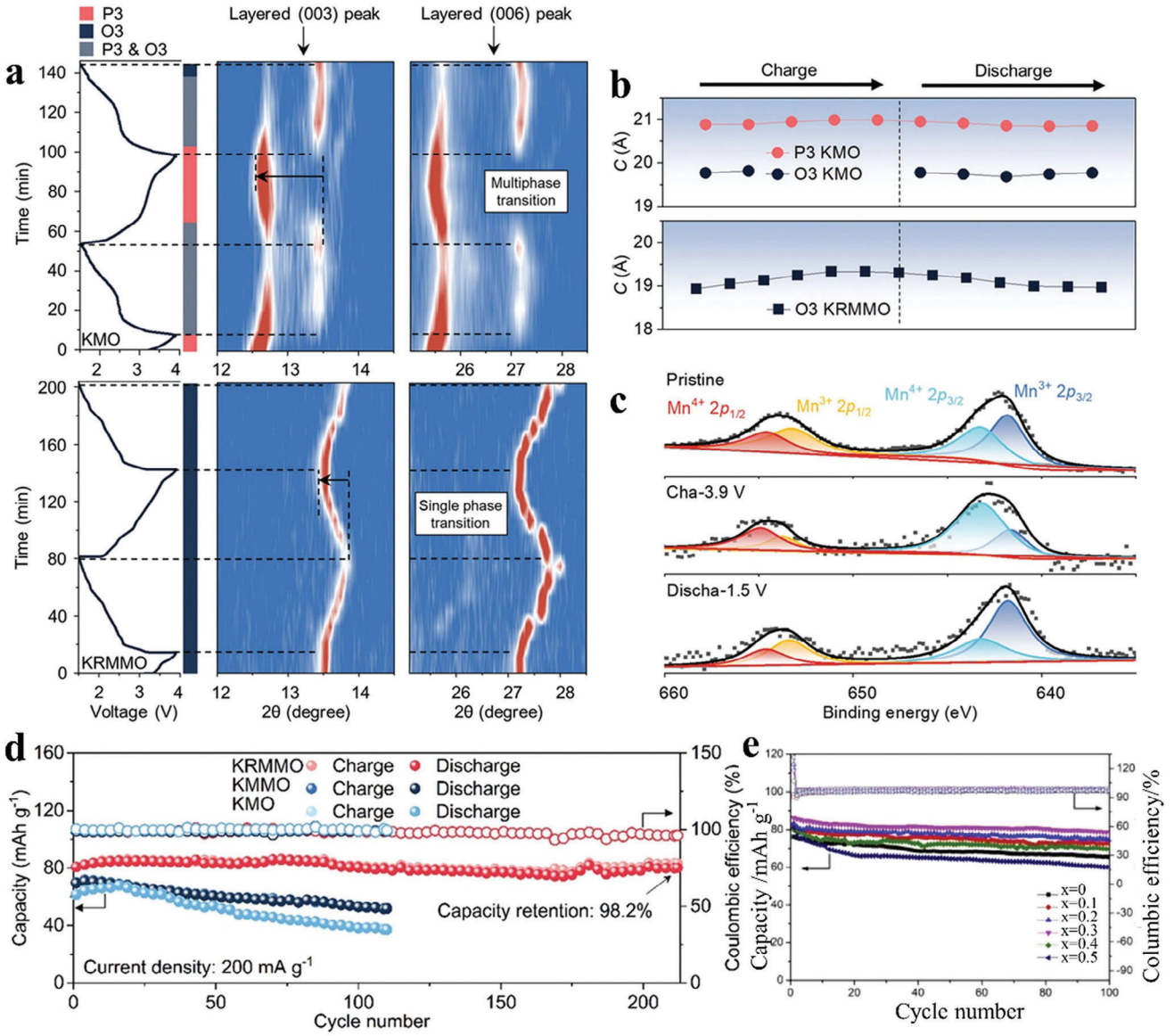

Figure 7. Structural evolution and charge compensation mechanism during a charge–discharge process. a) The voltage curves and representative corresponding in situ XRD patterns of KMO and KRMMO at 70 mA g^{-1} in the range of 1.5–3.9 V.[60] b) The c-lattice parameter of KMO and KRMMO calculated from in situ XRD patterns.[60] c) XPS spectra of Mn 2p at various states.[60] d) Cycling performance of KRMMO at 200 mA g^{-1}. a–d) Reproduced with permission.[60] Copyright 2022, Wiley-VCH. e) Cycling performance and coulombic efficiency of $K_{0.67-x}Na_xNi_{0.17}Co_{0.17}Mn_{0.66}O_2$ (x = 0, 0.1, 0.2, 0.3, 0.4, 0.5) at 20 mA g^{-1}. Reproduced with permission.[84] Copyright 2018, Pergamon-Elsevier Science Ltd.

stability as a PIB cathode material (**Figure** 7a–c). The synergistic effects of Rb and Mg substitutions facilitate the sliding of TM layers and suppress the transformation from the O3-type to P3-type host arrangement, thereby enhancing the structural robustness of KRMMO. Remarkably, the KRMMO cathode exhibits a high specific capacity of 108.0 mAh g^{-1} at 20 mA g^{-1} and 77.3 mAh g^{-1} at 500 mA g^{-1}, along with exceptional cycling stability, retaining 98.2% of its initial capacity after 200 cycles (Figure 7d). Notably, when compared to P3-$K_{0.5}MnO_2$, P3-KRMMO demonstrates significantly suppressed capacity fading, attributed to the collaborative effect of Rb and Mg ions in mitigating volume changes and suppressing phase transitions.

In a separate study, Liu et al.[84] utilized a co-precipitation method to synthesize a range of $K_{0.67-x}Na_xNi_{0.17}Co_{0.17}Mn_{0.66}O_2$ (x = 0, 0.1, 0.2, 0.3, 0.4, and 0.5) cathode materials and investigated the influence of Na content on their electrochemical performance. They observed that the crystalline structure transitioned from single phase to biphasic structure as the Na content increased. Moreover, Na substitution was found to enhance the stability of the layered structure and improve the reactivity of transition metal elements (Figure 7e). In conclusion, the substitution of Na in these cathode materials enhances the stability of the lamellar structure and promotes the reactivity of transition metal elements, leading to the suppression of Jahn-Teller distortion.

4.1.3. Substitutions at Anion Sites

The incorporation of anionic species at the O sites of MnO_6 has emerged as a promising approach to improve the electrochemical properties. This is attributed to the varying covalency of Mn—X interactions, where X represents an anion such as F^-, S^{2-}, and PO_4^{3-}, among others, due to their different electronegativities and radius. By introducing these species, the distortion of MnO_6 octahedra can be effectively suppressed.[9]

In LIBs, House et al.[85] conducted a notable study on the partial substitution of O^{2-} with F^- in $Li_{1.9}Mn_{0.95}O_{2.05}F_{0.95}$. The introduction of F^- anions into the cathode material increased the electronegativity, resulting in the reduction of the transition metal ion's valence. As a result, the F-substituted cathode material exhibited an impressive discharge capacity of 283 mAh g^{-1}, originating from both the Mn^{3+}/Mn^{4+} and anionic redox reactions. Additionally, the presence of the F^- anion in the cathode material suppressed oxygen loss associated with oxygen redox. Ex situ XRD analysis further confirmed the reversible extraction and insertion of Li^+ ions without significant structural changes of $Li_{1.9}Mn_{0.95}O_{2.05}F_{0.95}$, which features cation vacancies, eliminated the cooperative Jahn-Teller distortion commonly associated with Mn^{3+} in the ordered structure. This structural modification ultimately contributed to an enhanced long-term cycling stability.

In recent research, Xu et al.[61] made significant advancements in understanding the impact of anionic doping in layered oxides for PIBs, particularly in addressing capacity fading at high voltages (>4.0 V). By focusing on the P2-type $K_{2/3}Mn_{7/9}Ni_{1/9}Ti_{1/9}O_{17/9}F_{1/9}$ (KMNTOF) cathode, they demonstrated that the partial substitution of O^{2-} with F^- resulted in an increased interlayer distance in $K_{2/3}Mn_{7/9}Ni_{1/9}Ti_{1/9}O_2$ (KMNTO), facilitating faster K^+ transition without causing severe structural damage (**Figure 8a–c**). To evaluate the lattice stability of KMNTO and KMNTOF, changes in the c-axis parameter were calculated. The results, shown in Figure 8d,e, indicated that KMNTO exhibited a c-axis change (Δc) of 4% during the charge/discharge process, while KMNTOF showed a decreased value of Δc = 3.2%, indicating its improved tolerance to large-sized K^+ ions. The enhanced stability of KMNTOF can be attributed to two primary factors. First, the presence of Ni and Ti cations effectively mitigated the Jahn-Teller effect of Mn^{3+} and suppressed the detrimental sliding of TM layers during deep K^+ deintercalation. Additionally, the introduction of F^- anions expanded the interlayer distance along the c-axis direction from 6.31 to 6.33 Å, creating a more favorable environment for the (de)intercalation of large-sized K^+ ions while preserving the layered structure and preventing structural degradation. Moreover, experimental data and theoretical analysis confirmed that the incorporation of F^- anions increased the concentration of redox-active Mn cations, resulting in a higher reversible capacity derived from the $Mn^{3+/4+}$ redox couple rather than oxygen redox (Figure 8f–h). This anionic doping strategy enabled the KMNTOF cathode to exhibit an impressive reversible capacity of 132.5 mAh g^{-1}, with 0.53 K^+ reversible (de)intercalation in the structure. Therefore, the substitution of O^{2-} with the more electronegative F^- in KMO holds immense promise for enhancing working voltage and cycling stability in PIBs. These findings provide valuable insights into structural engineering approaches for the development of stable cathodes, thereby facilitating the future application of PIBs.

These findings highlight the promising potential of incorporating heteroatoms as a strategy to improve the electrochemical performance of emerging K_xMO_2 cathode materials in PIBs. The introduction of heteroatoms offers an effective approach to improve the stability and functionality of these cathode materials. However, further comprehensive analysis is needed to investigate the phase transition mechanism and optimize the material composition of layered K_xMO_2 for successful commercialization of these cathode materials. Continued research in this direction will contribute to the advancement and practical application of PIB technology.

4.2. Surface Coating

Surface coating has emerged as an effective and convenient approach to enhance electrochemical performance of Mn-based oxide cathodes in various applications. This is achieved by protecting the surface of Mn-based layered oxides, preventing undesirable electrolyte-electrode side reactions, mitigating the Jahn-Teller effect (Reduction in Mn^{2+} loss or reduction in Mn^{3+} content or reduced internal lattice expansion and contraction). This method involves the application of different coating agents, such as oxides, phosphates, fluorides, carbon, artificial solid-electrolyte interface (SEI), and conducting polymers. Extensive research has been conducted to investigate the impact of these surface modifications on the reversible capacity, cyclability (at both room and elevated temperatures), thermal stability, and other performance parameters of these cathodes.[20]

In a study conducted by Lei et al.,[23] a novel approach was proposed to improve the performance of K^+-layered materials through the creation of a dual interface structure comprising a K-poor spinel interlayer and a stable SEI film (**Figure 9a**). This dual interphase design serves multiple purposes (Figure 9b,c), inducing mitigating the Jahn-Teller distortion, reducing Mn^{2+} loss, and facilitating K^+ diffusion during redox reactions. Initially, the (002) and (004) diffraction peaks at 13.3° and 26.2°, respectively, represent the pristine state of P2-KMO. During charging, these peaks shift to lower angles, indicating an expansion in the distance between adjacent oxygen layers due to increased electrostatic repulsion. In deep charge stages, the (004) peak splits into two, signifying a two-phase reaction. A new peak at 25.6° represents the P″2 phase, which becomes dominant as the P2 phase decreases. Ultimately, at the end of charging, the P2 phase completely converts into the P″2 phase. These findings confirm a reversible process involving K^+ intercalation/deintercalation and a phase transition from P2 to P″2, consistent with charge/discharge profiles in Figure 9b (Figure 9d,e). The cycling performance of the modified P2-KMO in a 6.0 M KFSI/G2 electrolyte at a charge/discharge rate of 50 mA g^{-1} is depicted in Figure 9f. The material exhibits an initial capacity of 78.0 mAh g^{-1}, and notably, it maintains a high-capacity retention of 90.5% and Coulombic efficiency of 100% after 300 cycles, indicating exceptional stability. Figure 9g demonstrates the consistent voltage profiles of cathode during charge/discharge profiles over 100 cycles, further highlighting its reliability and performance consistency.

In another study, Wu et al.[86] fabricated a thin $K_3PO_4/MnPO_4$ layer on the surface of $K_{0.5}Mn_{0.8}Co_{0.2}O_2$ (KMCO), resulting in enhanced structural stability when utilized as cathodes for

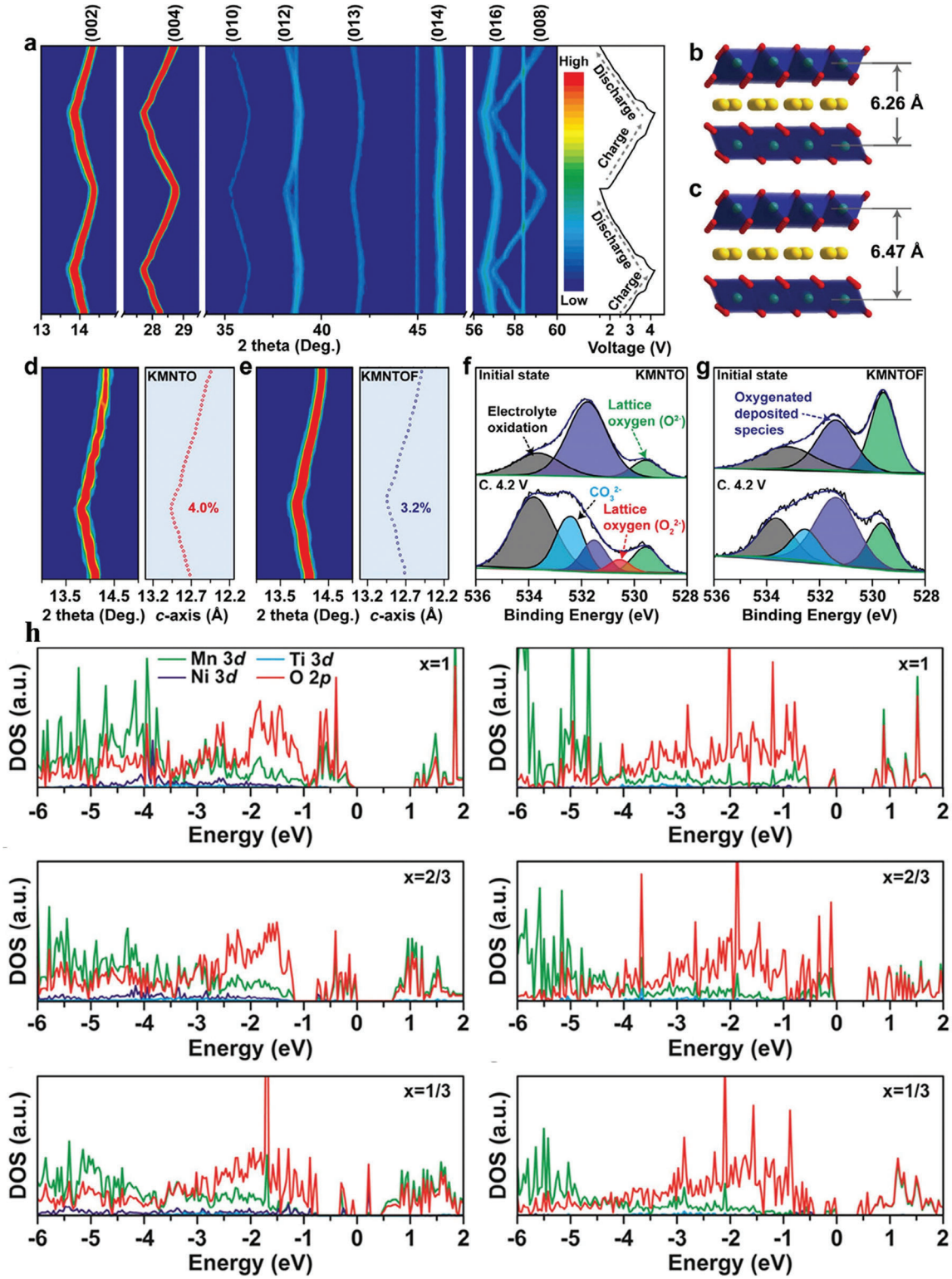

Figure 8. Structure evolution of KMNTO and KMNTOF upon K^+ (de)intercalation process. a) In situ XRD patterns for KMNTOF and corresponding charge/discharge profiles at 0.1 C.[61] b,c) Structure model of the layered KMNTOF at the states of discharged to 1.5 V and charged to 4.2 V, respectively.[61] d,e) In situ XRD patterns focused on the (002) lattice plane and corresponding c axis lattice parameters of KMNTO and KMNTOF, respectively.[61] f,g) XPS spectra of the KMNTO and KMNTOF samples, respectively. The peak of O^{2-} (529.5 eV) belonging to the crystalline framework and the peaks located at 531.6, 533.5, and 532.5 eV can be assigned to the adsorbed surface species.[61] h) First-principles calculations with the Fermi energy set to 0 eV. Reproduced with permission.[61] Copyright 2022, American Chemical Society.

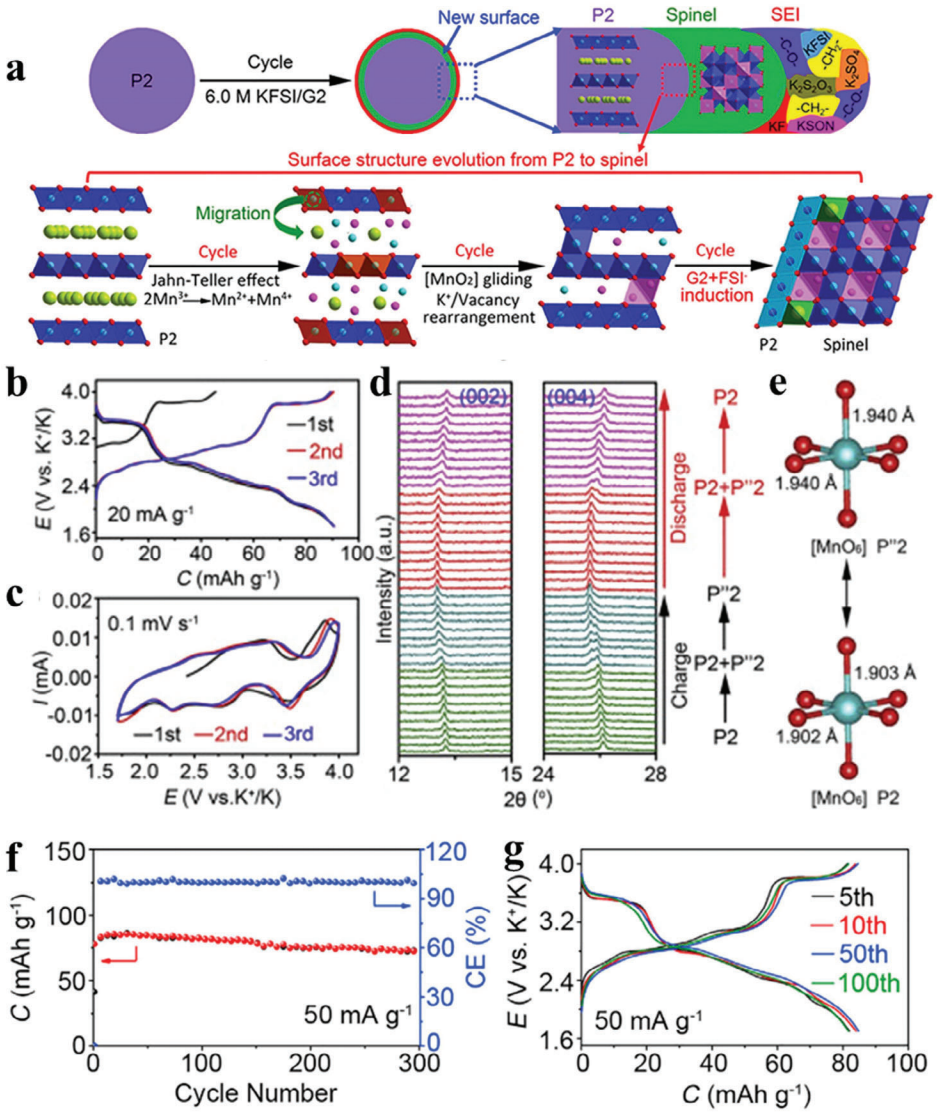

Figure 9. a) Schematic illustration of the formation of the dual interphase layers. Charge/Discharge Mechanism of P2-KMO Electrode in 6.0 M KFSI/G2. b) Charge/discharge curves of the initial 3 cycles at 20 mA g^{-1} between 1.7 and 4.0 V. c) CV curves of the initial 3 cycles at 0.1 mV s^{-1}. d) In situ XRD patterns recorded in the 1st cycle and the corresponding structure evolution of P2-KMO upon (de)potassiation. e) Mn—O bond length variation in the refined P"2 and P2 phases measured with Visualization for Electronic and Structural Analysis (VESTA) software. f) Cycle stability Performance of P2-KMO Electrode in 6.0 M KFSI/G2 at 50 mA g^{-1}. g) Selected charge/discharge profiles during the 5th, 10th, 50th, and 100th cycles at 50 mA g^{-1} between 1.7 and 4.0 V. a–f) Reproduced with permission[23] Copyright 2019, Elsevier.

PIBs. In comparison to pure KMCO, the $K_3PO_4/MnPO_4$-coated $K_{0.5}Mn_{0.8}Co_{0.2}O_2$ (P-KMCO) exhibits reduced surficial oxygen loss, a minimized layered-to-spinel-to-rock salt tri-phase transition and diminished internal lattice expansion and contraction during cycling. These observations were studied through aberration-corrected scanning transmission electron microscopy and in situ X-ray diffraction. This study highlights that surface coating is an effective strategy for developing stable cathodes for PIBs.

While surface coating has shown promise for improving the performance of K^+-layered materials, studies investigating this approach remain limited. Further research is needed to fully explore the potential and optimize the surface modification strategy for enhancing cathode materials. Continued investigations can provide valuable insights into the mechanisms and effectiveness of surface modifications, paving the way for the development of advanced cathode materials with enhanced electrochemical performance.[23]

4.3. Synthesis Strategies of K_xMO_2 for Suppressing the Jahn–Teller Effect

The synthesis methods employed for the preparation of electrode materials have a significant influence on the properties of energy storage devices. Various reaction parameters, such

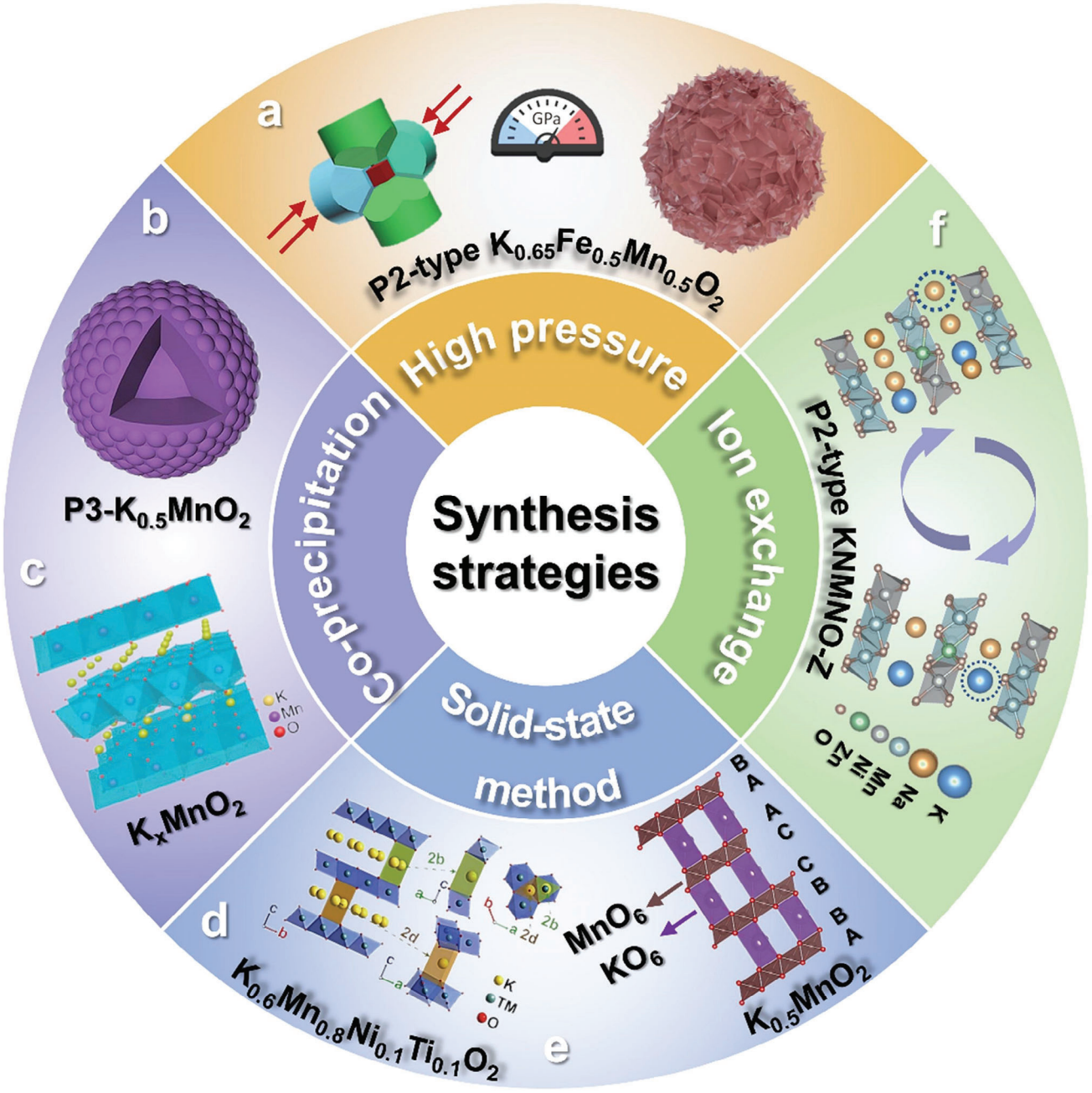

Figure 10. Schematic illustrations of synthesis strategies of K_xMO_2 for the suppression of the Jahn-Teller effect. a) High pressure synthesis strategy.[7] b) Co-precipitation synthesis strategy.[87] c) Co-precipitation synthesis strategy.[48] d) Solid-state method.[76] e) Solid-state method.[8] f) Ion exchange synthesis strategy.[59]

as temperature, time, pH, and precursor selection, play a crucial role in determining the structural characteristics of the materials, including crystallinity, particle size, surface morphology, composition, and phase purity. These structural characteristics, in turn, impact the electrochemical properties of electrode materials, including initial capacity, rate capability, and cyclic stability. Several methods are commonly used for the synthesis of electrode materials, including solid-state reactions, co-precipitation, high-pressure techniques, combustion methods, and electrochemical-ion exchange processes (**Figure 10**). Each method offers unique advantages and allows for control over different aspects of the material's properties (**Table 3**). By carefully fine-tuning the reaction parameters and utilizing multiple synthetic routes, it becomes possible to tailor the electrode materials to achieve desired stoichiometry, phase, morphology, and electrochemical properties.[18] The selection of appropriate synthesis methods and optimization of reaction conditions are crucial for the development of electrode materials with enhanced

Table 3. Summary of the advantages and disadvantages of synthetic methods.[18]

Methods	Advantages	Disadvantages
High pressure method	Simple and environmentally friendly	Limited by high-pressure vessel requirements and low product yields
Co-precipitation method	Uniform particle distribution and desired morphology	The precipitation agent, stirring speed, pH, and temperature must be adjusted
Solid-state method	Route is straightforward, suitable for mass production	Difficult to adjust the particle size and morphology of the active material
Ion exchange method	Enables the synthesis of unconventional intercalation compounds	The time-consuming and multistep procedure hinders its commercial viability
Sol–gel method	Lower processing temperature, uniform mixing of metal precursors	The pH of the solution must be controlled, precursor selection and reaction conditions control particle size
Combustion method	Simple and facile	Highly exothermic, produces potentially toxic fumes

electrochemical properties. Through systematic exploration and understanding of the synthesis-structure-performance relationships, researchers can advance the field of energy storage and contribute to the development of high-performance energy storage devices.

4.3.1. High Pressure Methods

To overcome the Jahn-Teller effect observed in Mn^{3+}-containing MnO_6 octahedra, the use of high-pressure synthesis has emerged as a promising strategy to suppress distortion without the need for additional interventions. By applying high pressure in combination with elevated temperatures, it becomes possible to reduce the lengths of the elongated Mn—O bonds within the octahedra, thereby increasing the energy barrier for structural rearrangement. This unique approach effectively mitigates the Jahn-Teller distortion and provides a novel pathway for its elimination.[9]

In LIBs, the introduction of Co as a substitution element offers a viable approach to stabilize the lattice structure of the rhombohedral $LiMnO_2$ (r-$LiMnO_2$) under high-pressure and high-temperature conditions, resulting in the formation of r-$LiMn_{0.36}Co_{0.64}O_2$.[88] This Co-substituted compound exhibits notable characteristics, including the absence of Jahn-Teller behavior and the potential for high-energy-density performance. However, it is crucial to consider the economic and industrial implications associated with the utilization of this strategy. The presence of electrochemically inactive phases and the substantial involvement of cobalt pose challenges that may limit the economic and industrial advantages of employing these Co-substituted materials in practical applications. The successful synthesis of P2-$K_{0.65}Fe_{0.5}Mn_{0.5}O_2$ (P2-KFMO) microspheres were using a modified solvent-thermal method under high-temperature and high-pressure conditions has demonstrated the elimination of Jahn-Teller distortion[7] This unique microsphere morphology, combined with the formation of a stable electrolyte intermediate phase during K^+ migration, has contributed to its exceptional electrochemical performance. The P2-KFMO microspheres exhibited a high reversible capacity of 151 mAh g^{-1} at 20 mA g^{-1} and demonstrated a remarkable capacity retention of 78% after 350 cycles. Furthermore, the porous structure of the P2-$K_{0.65}Fe_{0.5}Mn_{0.5}O_2$ microspheres, distinct from conventionally synthesized solid cathode materials, effectively mitigating excessive volume changes, leading to prolonged cycling performance.

The refinement of the high-pressure method is crucial for advancing the utilization of K_xMO_2 as cathode materials by effectively eliminating the Jahn-Teller distortion. Through further optimization and exploration of high-pressure synthesis techniques, it is possible to enhance the structural stability and electrochemical performance of K_xMO_2 materials, making them more suitable for practical applications in energy storage devices. K_xMO_2 materials, making them more suitable for practical applications in energy storage devices.

4.3.2. Co-Precipitation Method

The coprecipitation method is a versatile solution-based technique used for the synthesis of commercial cathode materials. It involves the production of a uniformly mixed metal ion precipitate using a precipitating agent, which is then mixed with an alkali metal source and subjected to high-temperature annealing to obtain the desired compound.[18] This method allows for precise control over the chemical compositions, particle sizes, morphologies of agglomerates, and "single-crystal" particles,[9] making it widely employed in cathode material synthesis.

For example, Peng et al.[87] successfully synthesized hollow P3-$K_{0.5}MnO_2$ nanospheres with an average diameter of 600 nm by precisely controlling the parameters of the coprecipitation reaction. The unique spherical morphology, along with the presence of interior voids, contributed to the high volumetric energy storage capacity and excellent cycling stability observed in the resulting P3-$K_{0.5}MnO_2$ cathode. Liu et al.[48] synthesized P2-$K_{0.3}MnO_2$ and P3-$K_{0.45}MnO_2$ cathodes using coprecipitation-assisted calcination. By adjusting the solution pH, temperature, and concentration during the coprecipitation process, they achieved a homogeneous particle distribution and desired morphology.[48] The smaller particle size of the P3-$K_{0.45}MnO_2$ cathode led to superior performance compared to P2-$K_{0.3}MnO_2$. In another study, Liu et al.[77] synthesized a $K_{0.67}Ni_{0.17}Co_{0.17}Mn_{0.66}O_2$ cathode using coprecipitation followed by a solid-state reaction The crystallinity of the resulting powder was observed to increase with higher sintering temperatures. Post heat treatment is often necessary to improve the crystallinity of compounds synthesized through coprecipitation methods. Precise adjustment of the precipitation agent, pH, stirring speed, and temperature is crucial to ensure the quality of the resulting products. These examples highlight the importance of controlling reaction parameters and post-processing conditions to achieve desired material properties in coprecipitation-based synthesis.

In summary, the co-precipitation approach demonstrates the potential to effectively mitigate the Jahn-Teller effect in layered

metal oxides. with stable lattices. By manipulating the synthesis parameters, such as pH and temperature, it becomes possible to control the morphological structures of the materials and tailor the valence states of manganese ions, resulting in the formation of stable lattices. These findings underscore the significance of the co-precipitation approach in reducing the Jahn-Teller distortions and enhancing the structural stability of the materials.

4.3.3. Solid-State Method

The solid-state reaction route is a commonly employed technique for synthesizing layered metal oxide cathodes for PIBs, offering simplicity and efficient production of cathode materials without Jahn-Teller behavior.[18] In a study by Liu et al.,[70] the effects of Fe doping on P3-$K_{0.45}Mn_{1-x}Fe_xO_2$ ($x \leq 0.5$) cathodes were investigated. The synthesis involved ball milling a stoichiometric mixture of K_2CO_3, Mn_2O_3, and Fe_2O_3 in ethanol for 12 h. Excess K_2CO_3 (5 wt.%) was added to compensate for potassium loss during high-temperature sintering. Pelletized mixtures were then sintered at 850 °C for 15 h. The cathode with the optimal performance was observed at a doping level of $x = 0.2$, while excessive doping ($x > 0.4$) resulted in impurities. These findings highlight the importance of optimizing dopant concentration to improve cathode structure and suppress the Jahn-teller effect. In a separate study, Kim et al.[8] utilized the conventional solid-state route to synthesize P3-$K_{0.5}MnO_2$ by employing K_2CO_3 and Mn_2O_3 precursors. The powders were stoichiometrically mixed, ball milled for 4 h, and calcined at 800 °C for 12 h to achieve the desired phase structure and crystallinity. Careful selection of appropriate precursors and precise control of calcination temperature are crucial for obtaining cathode materials without Jahn-Teller behavior using this method. Furthermore, Xu et al.[76] synthesized P2-$K_{0.6}Mn_{0.8}Ni_{0.1}Ti_{0.1}O_2$ by doping multiple elements. A pelletized mixture of K_2CO_3 (3 mol% excess), Mn_2O_3, NiO_2, and TiO_2 was calcined at 1000 °C for 15 h. The addition of Ni^{2+} and Ti^{4+} as dopants effectively suppressed lattice distortions caused by Mn^{3+} and hindered the gliding of the transition metal layer at high charged states, resulting in improved cathode performance.

Although the solid-state reaction route is a widely used method for synthesizing layered metal-oxide cathodes, it has limitations in terms of controlling particle size and morphology. The diffusion of alkali and transition metal ions through solid phases to achieve the desired crystal structure without impurities often requires prolonged, high-temperature calcination. Additionally, the physical mixing of precursors can result in non-uniform products with impurities. To address these challenges, there is a need for chemically controlled precursor formation under controlled conditions, enabling better control over the particle size and morphology of the resulting cathode materials.[18]

4.3.4. Ion Exchange Method

Ion exchange is a highly effective strategy for mitigating the Jahn-Teller effect by utilizing ions with similar ionic radius. In particular, the exchange of Na^+ (1.02 Å) and K^+ (1.37 Å) can eliminate the Jahn-Teller distortion without altering the crystal structure. This technique is widely employed for synthesizing metastable layered metal oxide compounds, as it enables the creation of intercalation compounds that cannot be easily obtained through conventional heat treatment methods. Ion exchange is commonly used in the preparation of cathodes for LIBs and SIBs, where the mobile ions in the host material are substituted with guest through immersion in Li or Na solutions or molten salts. Electrochemical ion exchange is another variation of this technique, where the ion exchange process occurs within an electrochemical battery during charged/discharged cycles in an electrolyte containing the target species. The solid-state synthesis of layered metal oxide compounds with high K^+ content poses challenges due to the strong repulsion between K^+ ions and the thermodynamically unstable conditions resulting from the large size of K^+ ions. However, the electrochemical ion-exchange technique shows great promise for the synthesis of K^+-layered cathodes with desired compositions.

According to recent reports, Choi has proposed P′2-$K_x[Ni_{0.05}Mn_{0.95}]O_2$ as a promising cathode material for PIBs.[67] The compound P′2-$K_{0.85}Na_{0.12}[Ni_{0.05}Mn_{0.95}]O_2$ was found to exhibit a notable absence of Jahn-Teller distortion, as observed from its structural behavior. Notably, the average oxidation state of Mn in this material closely approached Mn^{4+} (**Figure 11a**). P′2-$K_{0.83}[Ni_{0.05}Mn_{0.95}]O_2$ demonstrated a remarkable discharge capacity of 155 mAh g^{-1} (52 mA g^{-1}) and a high energy density of 420 Wh kg^{-1} within the voltage range of 1.5–4.3 V (Figure 11b,c). An interesting characteristic of the P′2-$K_{0.83}[Ni_{0.05}Mn_{0.95}]O_2$ structure is its rapid K-ion migration with a low activation barrier energy of ~271 meV, enabling high capacity at high currents and long-term cycling stability. Operando synchrotron X-ray diffraction analysis revealed that P′2-$K_{0.83}[Ni_{0.05}Mn_{0.95}]O_2$ maintained the P′2-phase without P′2-OP4 phase transition during charge/discharge in the voltage range of 1.5–4.3 V (Figure 11d,e). This is an unusual characteristic compared to other P′2-based layered cathode materials and is responsible for the long-term cycle stability of P′2-$K_{0.83}[Ni_{0.05}Mn_{0.95}]O_2$. First-principles calculations indicated that the excellent electrochemical performance can be attributed to the structural stability associated with a single-phase reaction upon K^+ extraction/insertion out of/into the host structure. Furthermore, XANES analysis was conducted during the de/potassiation process. In comparison to the reference spectra of $Mn^{3+}{}_2O_3$, $Mn^{4+}O_2$, and $Ni^{2+}O$, it was observed that de/potassiation resulted in a shift of the Mn and Ni K-edge spectra toward higher or lower photon energy, implying the participation of both Mn and Ni ions in the redox reaction. Specifically, the Mn oxidation state of $K_x[Ni_{0.05}Mn_{0.95}]O_2$ ($x = 0.10$) shifted toward Mn^{4+} upon charging, while the Mn oxidation state of $K_x[Ni_{0.05}Mn_{0.95}]O_2$ ($x = 0.83$, ~3.25+) was slightly higher than that of $Mn^{3+}{}_2O_3$, indicating a reduced influence of Jahn–Teller distortion by Mn^{3+} (Figure 11f–h).

The commercial viability of electrochemical ion exchange, despite its potential to produce advanced K^+-layered cathodes with enhanced characteristics, is hindered by its laborious and multistep nature, which could limit its practical application.

4.3.5. Sol–Gel Method

The sol-gel technique is a wet chemical process that involves the formation of a "sol" through the polymerization of metal salts in

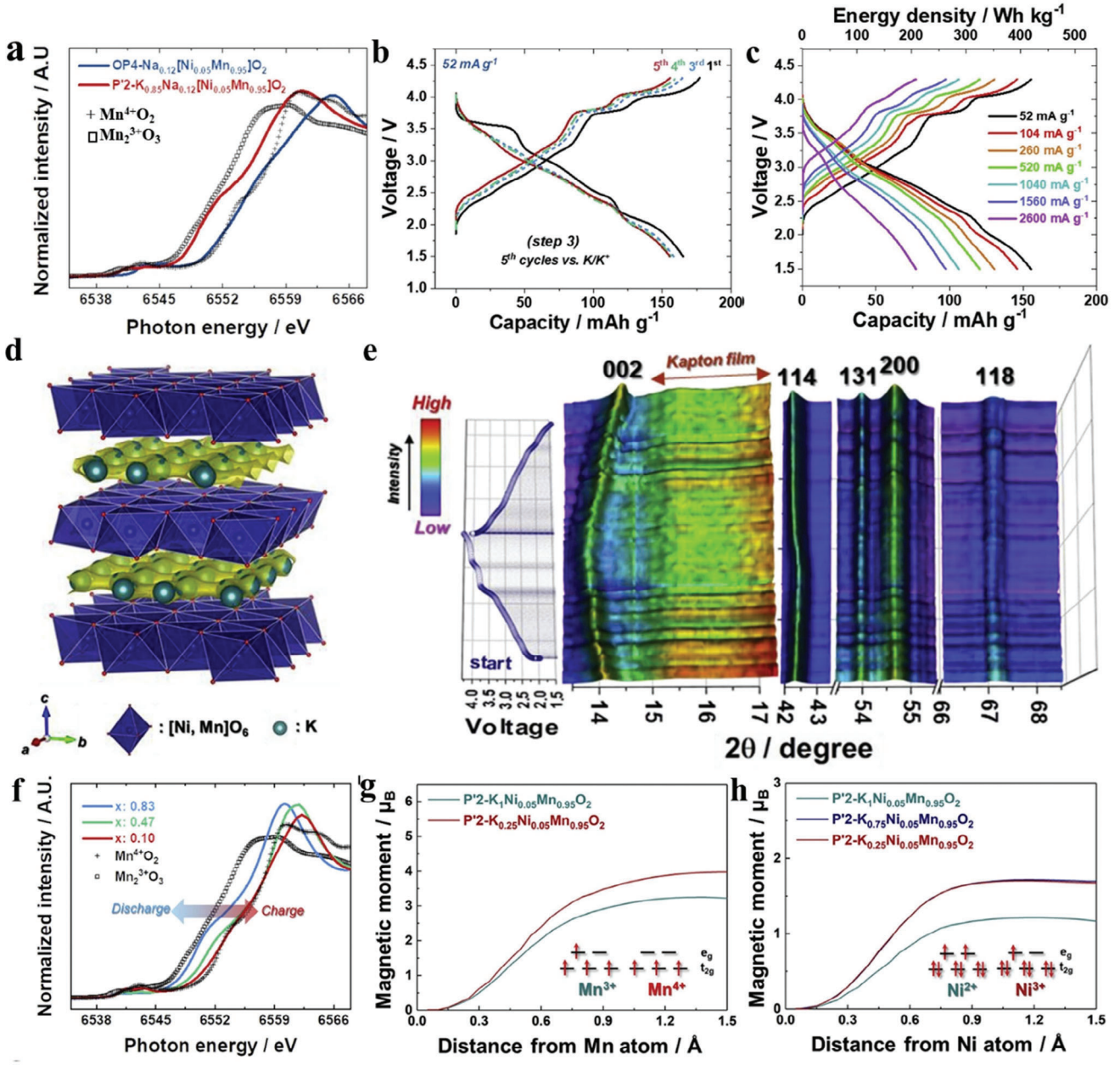

Figure 11. a) XANES spectra of Mn K-edge for 10th desodiated electrode and 1st potassiated electrode. b) Charge–discharge curves for the operating voltage range of 1.5–4.3 V P′2-$K_{0.83}[Ni_{0.05}Mn_{0.95}]O_2$. c) Voltage curves tested at various currents (52, 104, 260, 520, 1040, 1560, and 2600 mA g^{-1}) d) BVS energy landscape of P′2-$K_xNi_{0.05}Mn_{0.95}O_2$ that predicts possible K^+ atomic sites and diffusion paths. e) Operando synchrotron XRD patterns of $K_{0.83}[Ni_{0.05}Mn_{0.95}]O_2$; Kapton film: 17°–30°.[66] f) XANES spectra of Mn K-edge for $K_x[Ni_{0.05}Mn_{0.95}]O_2$ (x = 0.1–0.83) electrodes. Spin integration on g) Mn and h) Ni ions in P′2-$K_x[Ni_{0.05}Mn_{0.95}]O_2$. a–h) Reproduced with permission.[66] Copyright 2020, Elsevier.

a solvent, followed by the transformation of the sol into a porous "gel" network of colloidal particles. The gel is then dehydrated and subjected to heat treatment to obtain powders with the desired crystallinity. Parameters such as the chelating agent and solution pH play a crucial role in controlling the particle size, porosity, and morphology of the final product. Compared to conventional solid-state methods, the sol-gel method operates at lower processing temperatures, allowing for more uniform mixing of metal precursors. This synthesis stabilizes the material's structure, suppresses the deformation caused by Jahn-Teller, and enhances its electrochemical properties.

Lei et al.[23] reported the synthesis of a manganese-based P2-$K_{0.67}MnO_2$ cathode material using a sol-gel method. One notable feature of this material is the formation of a double-interface structure comprising a spinel interlayer and an organic/inorganic electrolyte phase film on the surface of 6.0 M of potassium bis(fluorosulfonyl)amide in diglyme (KFSI/G2). The cycling performance of P2-KMO in 6.0 M KFSI/G2 with a

charge/discharge rate of 50 mA g^{-1} demonstrated an initial capacity of 78 mAh g^{-1}. Remarkably, it exhibited high-capacity retention of 90.5% and Coulombic efficiency of 100% after 300 cycles, indicating excellent stability. The double-phase interlayer accommodates Jahn-Teller deformation, reduces Mn^{2+} loss, and improves K^+ diffusion of the redox reaction. Ultimately, this approach optimizes the electrochemical performance and stabilizes the structure of the materials. This study utilizes a spinel interlayer to protect the electrode material, effectively isolating it from the electrolyte and optimizing the battery's electrochemical performance.

In the sol-gel process, carful control of the solution pH is essential to prevent sol precipitation instead of gel formation. Additionally, achieving precise control over particle size during high-temperature heat treatment presents a challenge that requires careful selection of precursors and reaction conditions.

4.3.6. Combustion Method

The combustion method is employed to produce a finely mixed precursor or the desired active materials through spontaneous combustion between the reactants.[18] Further heating of the homogenous precursor mixture obtained from the combustion process allows for the synthesis of the desired product. In the study conducted by Cho et al.,[67] the synthesis of P3-$K_{0.5}[Ni_xMn_{1-x}]O_2$ (x = 0 and 0.1) was achieved through the combustion of metal nitrates. Citric acid and sucrose were used as a chelating agent and agglomeration inhibitor, respectively. In the compound $K_{0.5}MnO_2$, the oxidation state of Mn is found to be 3.5+, indicating the presence of Mn^{3+} ions known for their Jahn-Teller distortion in the oxide matrix. To investigate the influence of Ni doping on the Mn oxidation state and the Jahn-Teller effect, XANES analysis was conducted. The results confirmed the successful stabilization of introduced Ni ions as Ni^{2+} ions, as intended. This successful substitution of Mn^{3+} by Ni^{2+} resulted in a slight increase in the average oxidation state of Mn, effectively inhibiting the Jahn-Teller effect in the system. The P3-$K_{0.5}[Ni_{0.1}Mn_{0.9}]O_2$ cathode exhibited superior K^+ storage capacity and structural stability compared to the pristine cathode. It is important to note that while the combustion process is simple and convenient, it is an exothermic reaction that produce hazardous fumes, posing significant health and safety risks.

In conclusion, the selection of an appropriate approach is crucial for effectively suppressing the Jahn-Teller effect and advancing electrode materials with Jahn-Teller-free behavior. Various characterized by and fostering the progress of layered metal oxides. Various modified cathodes have demonstrated improved electrochemical properties, as summarized in **Table 4**. Doping with different elements has shown positive effects on voltage window, rate performance, and cycling stability, highlighting the efficacy of heteroatom substitution/doping. Structural and synthesis strategies, as well as surface coating, have also proven to be effective in suppressing the Jahn-Teller effect. However, further improvements are still necessary to overcome challenges such as complex phase transitions, Jahn-Teller effect, and disproportionation reactions of trivalent manganese during cycling, with the aim of enhancing capacity and structural stability for practical applications of these materials.

5. Conclusion and Perspective

5.1. Conclusion

Layered metal oxides have shown great potential as energy storage materials, but their practical application requires the development of Jahn-Teller-free variants that exhibit high structural stability, excellent long cycle life, and negligible voltage decay. Finding efficient methods to achieve these properties is currently a key focus in the field. This review offers a concise account of the origin and mechanism of the Jahn-Teller effect, coupled with proposed principles to mitigate this phenomenon. Specifically, we provide an overview of the current state of K_xMO_2 cathodes for PIBs, emphasizing the challenges posed by the Jahn-Teller effect. Additionally, we put forth promising strategies, including composition modulation, synthesis approaches, and surface coating, aimed at alleviating and suppressing the Jahn-Teller effect. These approaches not only provide valuable insights into the potential of innovative cathode materials but also establish a foundation for future research in the realm of PIBs.

In conclusion, the potential of PIBs systems as a promising large-scale energy storage solution, utilizing the abundant resource of potassium, has been established. Although there are current challenges that limit the commercial viability of PIBs, ongoing research aims to address these issues. It is important to discuss current PIBs technologies and identify new perspectives to enhance our understanding of PIBs system and expedite progress toward their practical application.

5.2. Perspective

Based on the above, future studies on the suppression of the Jahn-Teller effect in layered transition metal oxides can focus on the material design, characterization techniques, and theoretical calculations:

1) Material design

To meet future commercial demands, it is crucial to advance the design principles and synthesis methodologies of K_xMO_2 toward the development of stable materials. The structure of K_xMO_2 is susceptible to alteration due to the presence of water vapor in the air. Therefore, a proactive approach involves exploring novel layered oxide materials that lack Jahn-Teller distortion and exhibit good stability. This strategic combination can effectively prevent adverse reactions and establish a solid foundation for practical applications. The following manganese-based layered metal oxides serve as examples to propose potential avenues for future advancements.

a) Regulation of the valence state of Mn: Anticipating the future advancements in manganese-based cathode materials for applications, the precise regulation of manganese valence is projected to play a pivotal role in averting pronounced J-T effects and alleviating structural distortions. A promising avenue for achieving this control entails the strategic doping of elements (Ni, Mg, Zn, Ti) into K_xMnO_2, thereby raising the average valence state of Mn. Researchers envision that this method will continue to be a practical and effective means of tailoring the

Table 4. Electrochemical performance of layered oxide cathodes in half-cell PIBs.

Cathodes materials	Strategies	Voltage window [V]	Discharge capacity [mAh g^{-1}]/current density [mA g^{-1}]	Capacity retention [%] cycles/ current density [mA g^{-1}]	References
P3-$K_{0.45}Mn_{0.5}Co_{0.5}O_2$	Element doping	1.2–3.9	140/10	80/50/50	[62]
$K_{0.3}Mn_{0.95}Co_{0.05}O_2$	Element doping	2.0–3.6	99/22	75/500/173	[63]
$K_{0.54}[Co_{0.5}Mn_{0.5}]O_2$	Element doping	1.5–3.9	78/500	85/100/20	[5]
$K_{0.48}Mn_{0.4}Co_{0.6}O_2$	Element doping	1.0–4.2	64/C/20	81/180/C/10	[64]
$K_{0.75}[Ni_{1/3}Mn_{2/3}]O_2$	Element doping	1.5–4.5	110/20	83/500/1400	[65]
$K_{0.83}[Ni_{0.05}Mn_{0.95}]O_2$	Element doping	1.5–4.3	155/52	77/500/520	[66]
$K_{0.5}[Ni_{0.1}Mn_{0.9}]O_2$	Element doping	1.5–3.9	121/10	82/100/10	[67]
$K_{0.67}Ni_{0.17}Mn_{0.83}O_2$	Element doping	1.5–3.8	122/20	75/200/500	[68]
$K_{0.44}Ni_{0.22}Mn_{0.78}O_2$	Element doping	1.5–4.0	125.5/10	67/500/200	[2]
$K_{0.5}Mn_{0.7}Ni_{0.3}O_2$	Element doping	1.5–4.0	57.1/500	77/300/100	[69]
$K_{0.65}Fe_{0.5}Mn_{0.5}O_2$	Element doping	1.5–4.2	151/20	78/350/100	[7]
$K_{0.7}Fe_{0.5}Mn_{0.5}O_2$	Element doping	1.8–2.3	178/20	85/200/500	[46]
$K_{0.45}Mn_{0.8}Fe_{0.2}O_2$	Element doping	1.5–4.0	106.2/20	77.3/100/20	[70]
$K_{0.4}Fe_{0.5}Mn_{0.5}O_2$	Element doping	1.5–4.7	120/6	85/50/120	[27]
$K_{0.45}Mn_{0.9}Mg0._1O_2$	Element doping	1.5–4.0	108/20	74.8/100/20	[71]
$K_{0.54}Mn_{0.78}Mg_{0.22}O_2$	Element doping	1.5–4.0	132.4/20	84/100/200	[72]
$K_{0.7}Mn_{0.7}Mg_{0.3}O_2$	Element doping	1.5–4.0	144.5/20	82.5/400/100	[73]
$K_{5/9}Mn_{7/9}Ti_{2/9}O_2$	Element doping	1.5–4.2	130/20	~86/100/100	[74]
$K_{0.4}Fe_{0.1}Mn_{0.8}Ti_{0.1}O_2$	Element doping	1.8–4.0	117/20	74/300/200	[75]
$K_{0.6}Mn_{0.8}Ni_{0.1}Ti_{0.1}O_2$	Element doping	1.5—4.2	118/10	88/100/200	[76]
$K_{0.67}Ni_{0.17}Co_{0.17}Mn_{0.66}O_2$	Element doping	2.0–4.3	77/20	87/100/20	[77]
$K_{0.48}Ni_{0.2}Co_{0.2}Mn_{0.6}O_2$	Element doping	1.5–4.0	57/40	71/350/400	[78]
$K_{0.5}Mn_{0.72}Ni_{0.15}Co_{0.13}O_2$	Element doping	1.5–4.0	82.5/10	85/100/50	[79]
$K_{0.45}Ni_{0.1}Co_{0.1}Mg_{0.05}Mn_{0.8}O_2$	Element doping	1.5–4.0	79/10	74.3/100/20	[80]
$K_{0.45}Ni_{0.1}Co_{0.1}Al_{0.05}Mn_{0.8}O_2$	Element doping	1.5–4.0	79/10	77.4/100/20	[80]
$K_{0.75}[Mn_{0.8}Ni_{0.1}Fe_{0.1}]O_2$	Element doping	1.5–3.9	110/10	70/200/100	[81]
$K_{0.5}[Mn_{0.8}Fe_{0.1}Ni_{0.1}]O_2$	Element doping	1.5–3.9	120/50	74/300/50	[82]
$K_{1/2}Mn_{5/6}Mg_{1/12}Ni_{1/12}O_2$	Element doping	1.5–3.9	83.3/120	70.4/200/120	[83]
$K_{0.45}Rb_{0.05}Mn_{0.85}Mg_{0.15}O_2$	Element doping	1.5–3.9	108/20	98.2/200/200	[60]
$K_{0.37}Na_{0.3}Ni_{0.17}Co_{0.17}Mn_{0.66}O_2$	Element doping	2.0–4.2	86.1/20	91.5/100/20	[84]
$K_{2/3}Mn_{7/9}Ni_{1/9}Ti_{1/9}O_{17/9}F_{1/9}$	Element doping	15–4.2	54/500	91/50/100	[61]
$K_{0.67}MnO_2$	Surface coating	1.7–4.0	78/50	90.5/300/50	[23]
K_3PO_4/$MnPO_4$-coated KMCO	Surface coating	1.5–3.9	101.3/100	80/500/1000	[86]
$K_{0.65}Fe_{0.5}Mn_{0.5}O_2$	High pressure method	1.5–4.2	151/20	78/350/100	[7]
$K_{0.5}MnO_2$	Co-precipitation method	1.5–4.0	104/10	89.1/400/200	[87]
$K_{0.45}MnO_2$	Co-precipitation method	1.5–4.0	128.6/20	70.8/100/20	[48]
$K_{0.67}Ni_{0.17}Co_{0.17}Mn_{0.66}O_2$	Co-precipitation method	2.0–4.3	77/20	87/100/20	[77]
$K_{0.45}Mn_{0.8}Fe_{0.2}O_2$	Solid-state method	1.5–4.0	106.2/20	77.3/100/20	[70]
P3-$K_{0.5}MnO_2$	Solid-state method	1.5–3.9	97/10	70/50/20	[8]
$K_{0.6}Mn_{0.8}Ni_{0.1}Ti_{0.1}O_2$	Solid-state method	1.5–4.2	118/10	88/100/200	[76]
$K_{0.85}Na_{0.12}[Ni_{0.05}Mn_{0.95}]O_2$	Ion exchange method	1.5–4.3	181/26	-	[66]
$K_{0.67}MnO_2$	Sol–gel method	1.7–4.0	78/50	90.5/300/50	[23]
$K_{0.5}[Ni_{0.1}Mn_{0.9}]O_2$	Combustion	1.5–3.9	121/10	82/100/10	[67]

electrochemical properties of Mn-based layered oxides cathodes in future. Additionally, the integration of various components with different ratios could be explored to tune the Mn valence, fostering a stable structure of layered metal oxides, and suppressing the Jahn-Teller effect.

Furthermore, the introduction of Mn or O ionic vacancies emerges as an additional avenue with substantial potential. This approach is foreseen to contribute significantly to suppress J-T aberrations by constraining the elongation of bonds and finely adjusting the valence of Mn ions. As advancements in synthe-

sis techniques and theoretical understanding progress, the exploration of these strategies holds promise for the development of next-generation cathode materials with enhanced electrochemical performance, paving the way for more efficient and sustainable energy storage devices.

b) Appropriate coating agents need to be carefully chosen: Surface coating has become an efficient and convenient method to enhance the electrochemical performance of layered oxide cathodes across diverse applications. This involves safeguarding the surface of K_xMO_2, preventing undesirable electrolyte-electrode side reactions, and alleviating the Jahn-Teller effect. Appropriate coating agents, such as oxides, phosphates, fluorides, carbon, and conductive polymers, need to be carefully chosen. Despite the anticipated improvement in material stability through surface modification, research in this domain remains limited. Further investigations are essential to fully unlock the potential and optimize surface modification strategies for enhancing the stability of cathode materials.
c) Choosing optimal methods for synthesizing stable layered oxides: Embarking on varied synthesis methods to attain stable K_xMO_2. For instance, manipulating chemical bond lengths is achievable through high-pressure and/or high-temperature conditions, directly improving the symmetry of the octahedral MO_6. Consequently, the careful selection of an optimal method becomes paramount to efficiently suppress the Jahn-Teller effect and propel electrode materials toward Jahn-Teller-free behavior. Nevertheless, continuous enhancements are imperative to address persistent challenges, including intricate phase transitions and the Jahn-Teller effect during cycling. These improvements aim to boost capacity and structural stability, ensuring the practical viability of these materials.
d) Establishing structure-performance relationships: Establishing a robust structure-performance relationship is crucial for effectively guiding the production of K_xMO_2, thereby expanding the horizons of PIBs design. Presently, the study of the relationship between structure and performance is limited, and the properties associated with various material structures differ significantly. Consequently, there is a need for further investigation into the influence of material composition on structure, ultimately leading to the elucidation of the structure-activity relationship.

2) In-depth understanding of the reaction mechanism using advanced characterization technique

The electrochemical performance of cathode materials is intricately linked to internal structural properties or compositional changes during potassiation/depotassiation. A comprehensive understanding of their physicochemical transformations throughout the charge/discharge process is imperative for achieving high-performance PIBs. Nevertheless, conventional techniques fall short in accurately monitoring information, particularly for rapid processes that may generate unstable phases. Leveraging more dependable in situ spectroscopic characterization techniques, such as in situ X-ray absorption near-edge structure, in situ transmission electron microscopy, and in situ infrared spectroscopy, holds the potential to furnish compelling evidence. This, in turn, facilitates a deeper comprehension of the K^+ ion insertion/extraction process, offering intricate insights into interfacial reactions, K^+ ion transport, formation processes of the solid electrolyte interface, and the Jahn-Teller distortion phenomenon.

3) Theoretical calculations

A combination of theoretical calculations and machine learning serves as a valuable tool to enhance the fundamental understanding of the mechanism underlying K_xMO_2. For instance, molecular dynamics simulations and first-principles calculations offer detailed insights into the behavior of redox reactions at the molecular and atomic levels, respectively. Additionally, leveraging DFT calculations allows for the computation and analysis of adsorption energies of intermediates, unveiling the preferred reaction pathways of electrodes in each electrolyte. Moreover, the integration of artificial intelligence and machine learning is equally pivotal in predicting and optimizing the most rational material combinations, specifically stable K_xMO_2 cathodes devoid of Jahn-Teller aberrations, and in refining battery designs.

Acknowledgements

Y.Z. and H.X. contributed equally to this work. This work was funded by the Science and Technology Development Fund, Macau SAR (0033/2023/ITP1, 0022/2023/RIB1, 046/2019/AFJ, 0007/2021/AGJ, 0070/2023/AFJ, 006/2022/ALC), University of Macau (File no. MYRG2020-00187-IAPME, and MYRG2022-00223-IAPME) and the UEA funding.

Conflict of Interest

The authors declare no conflict of interest.

Keywords

cathode materials, Jahn–Teller effect, layered oxide, potassium-ion battery, strategies

Received: January 29, 2024
Published online:

[1] a) X. Zhang, Z. Wei, K. N. Dinh, N. Chen, G. Chen, F. Du, Q. Yan, *Small* **2020**, *16*, 2002700; b) S. Zhao, Z. Guo, K. Yan, X. Guo, S. Wan, F. He, B. Sun, G. Wang, *Small Struct.* **2020**, *2*, 2000054; c) S. Zhao, Z. Liu, G. Xie, Z. Guo, S. Wang, J. Zhou, X. Xie, B. Sun, S. Guo, G. Wang, *Energy Environ. Sci.* **2022**, *15*, 3015; d) W. Zuo, J. Qiu, X. Liu, F. Ren, H. Liu, H. He, C. Luo, J. Li, G. F. Ortiz, H. Duan, J. Liu, M. S. Wang, Y. Li, R. Fu, Y. Yang, *Nat. Commun.* **2020**, *11*, 3544; e) Z. Yu, Y. Xie, B. Xie, C. Cao, Z. Zhang, H. Huo, Z. Jiang, Q. Pan, G. Yin, J. Wang, *Energy Storage Mater.* **2020**, *25*, 416.
[2] X. Zhang, Y. Yang, X. Qu, Z. Wei, G. Sun, K. Zheng, H. Yu, F. Du, *Adv. Funct. Mater.* **2019**, *29*, 1 905 679.
[3] S. Zhao, K. Yan, P. Munroe, B. Sun, G. Wang, *Adv. Energy Mater.* **2019**, *9*, 1803757.
[4] T. Hosaka, K. Kubota, A. S. Hameed, S. Komaba, *Chem. Rev.* **2020**, *120*, 6358.
[5] J. U. Choi, J. Kim, J.-Y. Hwang, J. H. Jo, Y.-K. Sun, S. T. Myung, *Nano Energy* **2019**, *61*, 284.

[6] L. Deng, T. Wang, Y. Hong, M. Feng, R. Wang, J. Zhang, Q. Zhang, J. Wang, L. Zeng, Y. Zhu, L. Guo, *ACS Energy Lett.* **2020**, *5*, 1916.
[7] T. Deng, X. Fan, J. Chen, L. Chen, C. Luo, X. Zhou, J. Yang, S. Zheng, C. Wang, *Adv. Funct. Mater.* **2018**, *28*, 1800219.
[8] H. Kim, D. H. Seo, J. C. Kim, S. H. Bo, L. Liu, T. Shi, G. Ceder, *Adv. Mater.* **2017**, *29*, 1702480.
[9] S. Liu, B. Wang, X. Zhang, S. Zhao, Z. Zhang, H. Yu, *Matter* **2021**, *4*, 1511.
[10] Z. Yu, H. Shan, Y. Zhong, X. Zhang, G. Hong, *ACS Energy Lett.* **2022**, *7*, 3151.
[11] a) J. Wang, B. Wang, X. Liu, J. Bai, H. Wang, G. Wang, *Chem. Eng. J.* **2020**, *382*, 123050; b) X. Liu, Y. Cao, J. Sun, *Adv. Energy Mater.* **2022**, *12*, 2202532; c) Y. Liu, S. Fan, Y. Gao, Y. Liu, H. Zhang, J. Chen, X. Chen, J. Huang, X. Liu, L. Li, Y. Qiao, S. Chou, *Small* **2023**, *19*, 2302687; d) X. H. Liu, J. Peng, W. H. Lai, Y. Gao, H. Zhang, L. Li, Y. Qiao, S. L. Chou, *Adv. Funct. Mater.* **2021**, *32*, 2108616.
[12] a) Y. Lan, W. Yao, X. He, T. Song, Y. Tang, *Angew. Chem., Int. Ed.* **2020**, *59*, 9255; b) H. Li, C. Guan, M. Xu, J. Guo, K. Yuan, K. Cheng, Y. Xie, L. Zhang, J. Zheng, Y. Lai, Z. Zhang, *Energy Storage Mater.* **2022**, *47*, 526; c) H. Li, M. Xu, H. Long, J. Zheng, L. Zhang, S. Li, C. Guan, Y. Lai, Z. Zhang, *Adv. Sci.* **2022**, *9*, 2202082; d) K.-Y. Zhang, Z.-Y. Gu, E. H. Ang, J.-Z. Guo, X.-T. Wang, Y. Wang, X.-L. Wu, *Mater. Today* **2022**, *54*, 189.
[13] a) X. Yin, S. Sarkar, S. Shi, Q. A. Huang, H. Zhao, L. Yan, Y. Zhao, J. Zhang, *Adv. Funct. Mater.* **2020**, *30*, 1908445; b) X. Liu, Z. Ye, *Adv. Energy Mater.* **2020**, *11*, 2003281; c) J. Wang, G. Li, Q. Wang, L. Huang, X. Gan, M. Li, Z. Song, *Energy Storage Mater.* **2023**, *63*, 102956.
[14] a) H. Liu, W. Deng, X. Gao, J. Chen, S. Yin, L. Yang, G. Zou, H. Hou, X. Ji, *Nano Sel.* **2020**, *1*, 200; b) M. Chen, E. Wang, Q. Liu, X. Guo, W. Chen, S.-L. Chou, S.-X. Dou, *Energy Storage Mater.* **2019**, *19*, 163.
[15] X. Zhang, D. Yang, X. Rui, Y. Yu, S. Huang, *Curr. Opin. Electrochem.* **2019**, *18*, 24.
[16] Z. Wu, J. Zou, S. Chen, X. Niu, J. Liu, L. Wang, *J. Power Sources* **2021**, *484*, 229307.
[17] H. Park, Y. Lee, W. Ko, M. Choi, B. Ku, H. Ahn, J. Kim, J. Kang, J. K. Yoo, J. Kim, *Batteries Supercaps* **2023**, *6*, 202200486.
[18] M. G. T. Nathan, H. Yu, G. T. Kim, J. H. Kim, J. S. Cho, J. Kim, J. K. Kim, *Adv. Sci.* **2022**, *9*, 2105882.
[19] W. Li, Z. Bi, W. Zhang, J. Wang, R. Rajagopalan, Q. Wang, D. Zhang, Z. Li, H. Wang, B. Wang, *J. Mater. Chem. A* **2021**, *9*, 8221.
[20] L. Li, Z. Hu, Q. Liu, J.-Z. Wang, Z. Guo, H.-K. Liu, *Cell Rep. Phys. Sci.* **2021**, *2*, 100657.
[21] H. Peng, F. Xia, C. Zhang, H. Zhuo, X. Peng, P. Song, C. Sun, J. Wu, *Adv. Funct. Mater.* **2022**, *32*, 2113424.
[22] H. Kim, H. Ji, J. Wang, G. Ceder, *Trends Chem.* **2019**, *1*, 682.
[23] K. Lei, Z. Zhu, Z. Yin, P. Yan, F. Li, J. Chen, *Chem* **2019**, *5*, 3220.
[24] S. Liu, L. Kang, S. C. Jun, *Adv. Mater.* **2021**, *33*, 2004689.
[25] A. Manthiram, *Nat. Commun.* **2020**, *11*, 1550.
[26] a) R. E. Ruther, H. Zhou, C. Dhital, K. Saravanan, A. K. Kercher, G. Chen, A. Huq, F. M. Delnick, J. Nanda, *Chem. Mater.* **2015**, *27*, 6746; b) Z. Hu, M. Weng, Z. Chen, W. Tan, S. Li, F. Pan, *Nano Energy* **2021**, *83*, 105834; c) M.-H. Cao, Y. Wang, Z. Shadike, J.-L. Yue, E. Hu, S.-M. Bak, Y.-N. Zhou, X.-Q. Yang, Z.-W. Fu, *J. Mater. Chem. A* **2017**, *5*, 5442; d) H. Y. Asl, A. Manthiram, *Science* **2020**, *369*, 140; e) M. Holzapfel, O. Proux, P. Strobel, C. Darie, M. Borowski, M. Morcrette, *J. Mater. Chem.* **2004**, *14*, 102; f) S. Trushkin, S. W. Biernacki, L. Van Khoi, A. Kamińska, A. Suchocki, *New J. Phys.* **2008**, *10*, 013023.
[27] T. Masese, K. Yoshii, K. Tada, M. Kato, S. Uchida, K. Kubota, T. Ina, T. Okumura, Z.-D. Huang, J. Furutani, Y. Orikasa, H. Senoh, S. Tanaka, M. Shikano, *Energy Technol.* **2020**, *8*, 2000039.
[28] I. Bersuker, *The Jahn-Teller Effect*, Cambridge University Press, Cambridge **2009**.
[29] D. Reinen, *J. Solid State Chem.* **1979**, *27*, 71.
[30] H. Yaghoobnejad Asl, A. Manthiram, *J. Am. Chem. Soc.* **2020**, *142*, 21122.
[31] X. Li, Y. Wang, D. Wu, L. Liu, S.-H. Bo, G. Ceder, *Chem. Mater.* **2016**, *28*, 6575.
[32] a) J. A. Aramburu, P. García-Fernández, J. M. García-Lastra, M. Moreno, *J. Phys. Chem. C* **2017**, *121*, 5215; b) P. F. Wang, T. Jin, J. Zhang, Q. C. Wang, X. Ji, C. Cui, N. Piao, S. Liu, J. Xu, X. Q. Yang, C. Wang, *NanoEnergy* **2020**, *77*, 105167.
[33] C. C. C. M. C. M. O. Brien, *Am. J. Phys.* **1993**, *61*, 8.
[34] F. S. Ham, *Phys. Rev.* **1965**, *138*, A1727.
[35] P. Senn, *J. Chem. Educ.* **1992**, *69*, 819.
[36] a) D. reinen, *J. Solid State Chem.* **1976**, *27*, 71; b) S. V. Streltsov, D. I. Khomskii, *Physical Review X* **2020**, *10*, 031043.
[37] F. S. Ham, *Phys. Rev.* **1968**, *166*, 307.
[38] W. J. Kim, M. A. Smeaton, C. Jia, B. H. Goodge, B. G. Cho, K. Lee, M. Osada, D. Jost, A. V. Ievlev, B. Moritz, L. F. Kourkoutis, T. P. Devereaux, H. Y. Hwang, *Nature* **2023**, *615*, 237.
[39] a) W. Li, E. M. Erickson, A. Manthiram, *Nat. Energy* **2020**, *5*, 26; b) J. Liu, Z. Bao, Y. Cui, E. J. Dufek, J. B. Goodenough, P. Khalifah, Q. Li, B. Y. Liaw, P. Liu, A. Manthiram, Y. S. Meng, V. R. Subramanian, M. F. Toney, V. V. Viswanathan, M. S. Whittingham, J. Xiao, W. Xu, J. Yang, X.-Q. Yang, J.-G. Zhang, *Nat. Energy* **2019**, *4*, 180.
[40] J. L. Pimlott, R. J. Street, M. P. Down, C. E. Banks, *Adv. Funct. Mater.* **2021**, *31*, 2107761.
[41] F. Ding, C. Zhao, D. Xiao, X. Rong, H. Wang, Y. Li, Y. Yang, Y. Lu, Y. S. Hu, *J. Am. Chem. Soc.* **2022**, *144*, 8286.
[42] Z. Liu, H. Su, Y. Yang, T. Wu, S. Sun, H. Yu, *Energy Storage Mater.* **2021**, *34*, 211.
[43] Y.-S. Xu, S.-Y. Duan, Y.-G. Sun, D.-S. Bin, X.-S. Tao, D. Zhang, Y. Liu, A.-M. Cao, L.-J. Wan, *J. Mater. Chem. A* **2019**, *7*, 4334.
[44] X. Min, J. Xiao, M. Fang, W. Wang, Y. Zhao, Y. Liu, A. M. Abdelkader, K. Xi, R. V. Kumar, Z. Huang, *Energy Environ. Sci.* **2021**, *14*, 2186.
[45] a) M. Ren, S. Zhao, S. Gao, T. Zhang, M. Hou, W. Zhang, K. Feng, J. Zhong, W. Hua, S. Indris, K. Zhang, J. Chen, F. Li, *J. Am. Chem. Soc.* **2023**, *145*, 224; b) M. Ren, Z. Zhu, Z. Liang, Y. Huang, T. Zhang, M. Hou, K. Zhang, Z. Chen, Y. He, Z. Ma, J. Chen, F. Li, *Small* **2023**, *19*, 2304187.
[46] X. Wang, X. Xu, C. Niu, J. Meng, M. Huang, X. Liu, Z. Liu, L. Mai, *Nano Lett.* **2017**, *17*, 544.
[47] C. Vaalma, G. A. Giffin, D. Buchholz, S. Passerini, *J. Electrochem. Soc.* **2016**, *163*, A1295.
[48] C.-L. Liu, S.-H. Luo, H.-B. Huang, Y.-C. Zhai, Z.-W. Wang, *Chem. Eng. J.* **2019**, *356*, 53.
[49] R.-J. Luo, X.-L. Li, J.-Y. Ding, J. Bao, C. Ma, C.-Y. Du, X.-Y. Cai, X.-J. Wu, Y.-N. Zhou, *Energy Storage Mater.* **2022**, *47*, 408.
[50] I. B. Bersuker, *Chem. Rev.* **2021**, *121*, 1463.
[51] J. Zhang, J. B. Kim, J. Zhang, G. H. Lee, M. Chen, V. W. Lau, K. Zhang, S. Lee, C. L. Chen, T. Y. Jeon, Y. W. Kwon, Y. M. Kang, *J. Am. Chem. Soc.* **2022**, *144*, 7929.
[52] S. C. Han, W. B. Park, K.-S. Sohn, M. Pyo, *J. Solid State Electrochem.* **2019**, *23*, 3135.
[53] Y. W. Ming-Hui Cao, Z. Shadike, J.-L. Yue, E. Hu, S.-M. Bak, Y.-N. Zhou, X.-Q. Yang, Z.-W. Fu, *J. Mater. Chem. A* **2017**, *5*, 5442.
[54] E. J. Kim, P. R. Kumar, Z. T. Gossage, K. Kubota, T. Hosaka, R. Tatara, S. Komaba, *Chem. Sci.* **2022**, *13*, 6121.
[55] H. Kim, D.-H. Seo, A. Urban, J. Lee, D.-H. Kwon, S.-H. Bo, T. Shi, J. K. Papp, B. D. McCloskey, G. Ceder, *Chem. Mater.* **2018**, *30*, 6532.
[56] J.-Y. Hwang, J. Kim, T.-Y. Yu, S.-T. Myung, Y.-K. Sun, *Energy Environ. Sci.* **2018**, *11*, 2821.
[57] N. Naveen, S. C. Han, S. P. Singh, D. Ahn, K.-S. Sohn, M. Pyo, *J. Power Sources* **2019**, *430*, 137.
[58] K. Kubota, S. Kumakura, Y. Yoda, K. Kuroki, S. Komaba, *Adv. Energy Mater.* **2018**, *8*, 1703415.

[59] Y. Zheng, J. Li, S. Ji, K. S. Hui, S. Wang, H. Xu, K. Wang, D. A. Dinh, C. Zha, Z. Shao, K. N. Hui, *Small* **2023**, *19*, 2302160.
[60] Z. Caixiang, J. Hao, J. Zhou, X. Yu, B. Lu, *Adv. Energy Mater.* **2022**, *13*, 2203126.
[61] Y. S. Xu, M. Y. Qi, Q. H. Zhang, F. Q. Meng, Y. N. Zhou, S. J. Guo, Y. G. Sun, L. Gu, B. B. Chang, C. T. Liu, A. M. Cao, L. J. Wan, *ACS Appl. Mater. Interfaces* **2022**, *14*, 13379.
[62] H. V. Ramasamy, B. Senthilkumar, P. Barpanda, Y.-S. Lee, *Chem. Eng. J.* **2019**, *368*, 235.
[63] Q. Zhang, C. Didier, W. K. Pang, Y. Liu, Z. Wang, S. Li, V. K. Peterson, J. Mao, Z. Guo, *Adv. Energy Mater.* **2019**, *9*, 1900568.
[64] K. Sada, P. Barpanda, *Chem. Commun. (Camb)* **2020**, *56*, 2272.
[65] J. H. Jo, J. U. Choi, Y. J. Park, Y. H. Jung, D. Ahn, T. Y. Jeon, H. Kim, J. Kim, S. T. Myung, *Adv. Energy Mater.* **2020**, *10*, 1903605.
[66] J. U. Choi, Y. Ji Park, J. H. Jo, Y. H. Jung, D.-C. Ahn, T.-Y. Jeon, K.-S. Lee, H. Kim, S. Lee, J. Kim, S.-T. Myung, *Energy Storage Mater.* **2020**, *27*, 342.
[67] M. K. Cho, J. H. Jo, J. U. Choi, S. T. Myung, *ACS Appl. Mater. Interfaces* **2019**, *11*, 27770.
[68] P. Bai, K. Jiang, X. Zhang, J. Xu, S. Guo, H. Zhou, *ACS Appl. Mater. Interfaces* **2020**, *12*, 10490.
[69] L. Duan, J. Xu, Y. Xu, R. Tian, Y. Sun, C. Zhu, X. Mo, X. Zhou, *J. Energy Chem.* **2023**, *76*, 332.
[70] C.-L. Liu, S.-H. Luo, H.-B. Huang, X. Liu, Y.-C. Zhai, Z.-W. Wang, *Chem. Eng. J.* **2019**, *378*, 122167.
[71] C. L. Liu, S. H. Luo, H.-B. Huang, Y.-C. Zhai, Z.-W. Wang, *ChemElectroChem* **2019**, *6*, 2308.
[72] R. Huang, Q. Xue, J. Lin, X. Zhang, J. Zhou, F. Wu, L. Li, R. Chen, *Nano Res.* **2021**, *15*, 3143.
[73] J. Weng, J. Duan, C. Sun, P. Liu, A. Li, P. Zhou, J. Zhou, *Chem. Eng. J.* **2020**, *392*, 123649.
[74] Y.-S. Xu, Q.-H. Zhang, D. Wang, J.-C. Gao, X.-S. Tao, Y. Liu, Y.-G. Sun, L. Gu, B.-B. Chang, C.-T. Liu, S.-Q. Shi, A.-M. Cao, *Energy Storage Mater.* **2020**, *31*, 20.
[75] X. Zhang, D. Yu, Z. Wei, N. Chen, G. Chen, Z. X. Shen, F. Du, *ACS Appl. Mater. Interfaces* **2021**, *13*, 18897.
[76] Y.-S. Xu, Y.-N. Zhou, Q.-H. Zhang, M.-Y. Qi, S.-J. Guo, J.-M. Luo, Y.-G. Sun, L. Gu, A.-M. Cao, L.-J. Wan, *Chem. Eng. J.* **2021**, *412*, 128735.
[77] C. Liu, S. Luo, H. Huang, Z. Wang, A. Hao, Y. Zhai, Z. Wang, *Electrochem. Commun.* **2017**, *82*, 150.
[78] S. Xu, C. Bao, M. Yu, S. Liu, L. Chen, D. Zhang, *Mater. Lett.* **2020**, *270*, 127733.
[79] Q. Deng, F. Zheng, W. Zhong, Q. Pan, Y. Liu, Y. Li, G. Chen, Y. Li, C. Yang, M. Liu, *Chem. Eng. J.* **2020**, *392*, 123735.
[80] R. Dang, N. Li, Y. Yang, K. Wu, Q. Li, Y. L. Lee, X. Liu, Z. Hu, X. Xiao, *J. Power Sources* **2020**, *464*, 228190.
[81] J.-Y. Hwang, J. Kim, T.-Y. Yu, H.-G. Jung, J. Kim, K.-H. Kim, Y.-K. Sun, *J. Mater. Chem. A* **2019**, *7*, 21362.
[82] J. U. Choi, J. Kim, J. H. Jo, H. J. Kim, Y. H. Jung, D.-C. Ahn, Y.-K. Sun, S.-T. Myung, *Energy Storage Mater.* **2020**, *25*, 714.
[83] L. Liu, J. Liang, W. Wang, C. Han, Q. Xia, X. Ke, J. Liu, Q. Gu, Z. Shi, S. Chou, S. Dou, W. Li, *ACS Appl. Mater. Interfaces* **2021**, *13*, 28369.
[84] C.-L. Liu, S.-H. Luo, H.-B. Huang, Y.-C. Zhai, Z.-W. Wang, *Electrochim. Acta* **2018**, *286*, 114.
[85] R. A. House, L. Jin, U. Maitra, K. Tsuruta, J. W. Somerville, D. P. Förstermann, F. Massel, L. Duda, M. R. Roberts, P. G. Bruce, *Energy Environ. Sci.* **2018**, *11*, 926.
[86] H. Wang, H. Peng, Z. Xiao, R. Yu, F. Liu, Z. Zhu, L. Zhou, J. Wu, *Energy Storage Mater.* **2023**, *58*, 101.
[87] B. Peng, Y. Li, J. Gao, F. Zhang, J. Li, G. Zhang, *J. Power Sources* **2019**, *437*, 226913.
[88] T. Uyama, K. Mukai, I. Yamada, *Inorg. Chem.* **2019**, *58*, 6684.

Yunshan Zheng is a doctoral candidate in the Department of IAPME at University of Macau, China. Her research interests include the construction of micro-nano materials, lithium, sodium, and potassium-ion battery.

Huixian Xie obtained both her bachelor's and master's degrees from Guangdong University of Technology in 2019 and 2022 respectively. She is now a Ph.D. student in University of Macau. Her current research interests focus on the electrochemical energy storage, including Li-ion, Na-ion, and K-ion batteries.

Junfeng Li received his Ph.D. degree from the University of Macau in 2023. He currently is a postdoctoral researcher at Tsinghua Shenzhen International Graduate School, Tsinghua University. His research focuses on preparing advanced electrode materials and the design of battery systems, including aluminum-ion batteries and potassium-ion batteries.

Kwan San Hui is a reader in mechanical engineering of School of Engineering, University of East Anglia. He obtained his Ph.D. degree in mechanical engineering at the Hong Kong University of Science and Technology (2008). His research focuses on advanced materials for energy storage, conversion, and electrocatalysis.

Zhenjiang Yu is a postdoctoral in the University of Macau and research fellow in the Lancaster University. His research interests include the alkali (lithium, sodium, and potassium) ion battery, solid-state battery, and X-ray imaging.

Huifang Xu is a doctoral candidate in the Department of IAPME at University of Macau, China. Her research interests include the construction of micro-nano materials, lithium, sodium, and potassium-ion battery.

Duc Anh Dinh achieved his Ph.D. degree in the field of chemistry of materials at Italian Institute of Technology and Genova university, Italy in 2018. Currently, he is a researcher, working at Nguyen Tat Thanh hi-tech institute, Nguyen Tat Thanh university Vietnam. His research interest is focusing in two fields: 1) production and processing of graphene and related 2D materials for energy storage, sensors and electronic devices; 2) synthesis and characterization of biodegrade polymers.

Zhengqing Ye is an associate professor of the School of Material Science and Engineering, Hebei University of Technology. He obtained his Ph.D. degree from Beijing Institute of Technology. He is Macao Young Scholar and Yuanguang Scholar of Hebei University of Technology. His research interests focus on electrocatalysis, secondary batteries and other electrochemical energy storage materials and devices.

Chenyang Zha is working at the Institute of Applied Physics and Materials Engineering (IAPME) of University of Macau. He received his Ph.D. degree in chemistry from Nanjing Tech University and Uppsala University in 2016, and then he moved to Soochow University and the State University of New York to complete postdoctoral training before taking the current position in 2020. His research focuses on novel functional materials for energy applications, particularly in the realm of advanced batteries and electrocatalysts.

Kwun Nam Hui is an associate professor of the Institute of Applied Physics and Materials Engineering, University of Macau. He obtained his Ph.D. degree from The University of Hong Kong (2009). His research focuses on electrochemical energy storage and conversion.